



# How fluid infiltrates dry crustal rocks during progressive eclogitization and shear zone formation: insights from H<sub>2</sub>O contents in nominally anhydrous minerals

Lisa Kaatz<sup>1</sup> · Julien Reynes<sup>2</sup> · Jörg Hermann<sup>3</sup> · Timm John<sup>1</sup>

Received: 28 January 2022 / Accepted: 4 July 2022 / Published online: 18 July 2022  
© The Author(s) 2022

## Abstract

Granulites from Holsnøy (Bergen Arcs, Norway) maintained a metastable state until fluid infiltration triggered the kinetically delayed eclogitization. Interconnected hydrous eclogite-facies shear zones are surrounded by unreacted granulites. Macroscopically, the granulite–eclogite interface is sharp and there are no significant compositional changes in the bulk chemistry, indicating the fluid composition was quickly rock buffered. To better understand the link between deformation, fluid influx, and fluid–rock interaction one cm-wide shear zone at incipient eclogitization is studied here. Granulite and eclogite consist of garnet, pyroxene, and plagioclase. These nominally anhydrous minerals (NAMs) can incorporate H<sub>2</sub>O in the form of OH groups. H<sub>2</sub>O contents increase from granulite to eclogite, as documented in garnet from ~ 10 to ~ 50 µg/g H<sub>2</sub>O, pyroxene from ~ 50 to ~ 310 µg/g H<sub>2</sub>O, and granulitic plagioclase from ~ 10 to ~ 140 µg/g H<sub>2</sub>O. Bowl-shape profiles are characteristic for garnet and pyroxene with lower H<sub>2</sub>O contents in grain cores and higher at the rims, which suggest a prograde water influx into the NAMs. Omphacite displays a H<sub>2</sub>O content range from ~ 150 to 425 µg/g depending on the amount of hydrous phases surrounding the grain. The granulitic plagioclase first separates into a hydrous, more albite-rich plagioclase and isolated clinozoisite before being replaced by new fine-grained phases like clinozoisite, kyanite and quartz during ongoing fluid infiltration. Results indicate a twofold fluid influx with different mechanisms to act simultaneously at different scales and rates. Fast and more pervasive proton diffusion is recorded by NAMs that retain the major element composition of the granulite-facies equilibration where hydrogen decorates pre-existing defects in the crystal lattice and leads to OH increase. Contemporaneously, slower grain boundary-assisted aqueous fluid influx enables element transfer and results in progressive formation of new minerals, e.g., hydrous phases. Both mechanisms lead to bulk H<sub>2</sub>O increase from ~ 450 to ~ 2500 µg/g H<sub>2</sub>O towards the shear zone and convert the system from rigid to weak. The incorporation of OH groups reduces the activation energy for creep, promotes formation of smaller grain sizes (phase separation of plagioclase), and synkinematic metamorphic mineral reactions. These processes are part of the transient weakening, which enhance the sensitivity of the rock to deform.

**Keyword** Water in NAMs · Eclogitization · Shear zone formation · Rock weakening · Fluid–rock interaction

---

Communicated by Gordon Moore.

✉ Lisa Kaatz  
lisa.kaatz@fu-berlin.de

✉ Timm John  
timm.john@fu-berlin.de

<sup>1</sup> Institute of Geological Sciences, Freie Universität Berlin, 12249 Berlin, Germany

<sup>2</sup> Institute of Earth Sciences, University of Lausanne, CH-1015 Lausanne, Switzerland

<sup>3</sup> Institute of Geological Sciences, University of Bern, CH-3012 Bern, Switzerland

## Introduction

Convergent plate boundaries reflect Earth's most dynamic systems. Various highly interconnected processes occur on a large range of timescales and spatial scales, such as metamorphism and deformation. Exposed field examples and geophysical imaging reveal that during subduction and continental collision dry lower crustal rocks may behave stiff and rigid, although they are affected by changing pressure (P) and temperature (T) conditions and deformation (e.g., Rondenay et al. 2008; Yuan et al. 2000). Such rocks remain in a metastable state until fluid infiltration triggers the kinetically delayed transformation from dry to partly hydrous

assemblages (e.g., Austrheim 1987; John and Schenk 2003). Detailed field studies have shown that brittle deformation enables fluid to infiltrate these metastable regions through fractures and seismic fault planes (e.g., Austrheim 1987; Jamtveit et al. 2019). This fluid supply then provokes the rock weakening by progressive mineral transformation, which, in turn, favors ductile deformation (e.g., Austrheim 1998; Kaatz et al. 2021; Putnis and Austrheim 2010). The weakening itself is associated with the recrystallization of fine-grained metamorphic minerals and reduction of the activation energy for creep caused by traces of water in the crystal lattices (e.g., Hawemann et al. 2019; Kohlstedt 2006; Menegon et al. 2017; Putnis and John 2010). It has been shown that under such circumstances widening of the shear zone overcomes the effect of stretching during progressive fluid–rock interaction and strain accumulation (Kaatz et al. 2021). A continuous supply of fluid which infiltrates the system through, e.g., fractures, can be either ensured by numerous repetitive pulses and/or by a substantial amount of infiltrating fluid. This fluid infiltration then has a strong positive effect on shear zone widening (e.g., Kaatz et al. 2021).

What is still missing in this feedback mechanism is a good understanding on how fluid infiltrates the rock during deformation of the crust at eclogite-facies P–T conditions. To extract this information, a study was conducted on rocks that display an early stage of shear zone formation accompanied by partial eclogitization likely caused by the infiltration of an aqueous fluid. The mineral assemblages of dry deep crustal rocks, e.g., of granulite, often consist of garnet, pyroxene, and plagioclase. These minerals are nominally anhydrous minerals (NAMs), but can incorporate tens to hundreds  $\mu\text{g/g}$   $\text{H}_2\text{O}$  in the form of OH groups, where H substitutes for cations (Bell et al. 1995; Bromiley and Keppler 2004; Johnson 2006; Koch-Müller et al. 2004). This study focuses on both the quantification and spatial distribution of OH in these NAMs as well as minor high-pressure hydrous phases to explore the mechanisms leading to hydration of a dry granulite wall rock during the formation of an eclogite-facies mineral assemblage. The hydration of NAMs and formation of hydrous phases might highly influence the weakening, deformation, rheology, and metamorphism of the rock during subduction.

## Geological setting and samples

The closure of the Iapetus ocean initiated the collision of Baltica and Laurentia at  $\sim 430$  Ma (e.g., Corfu et al. 2014; Roberts 2003). Consequently, parts of Baltica subducted underneath Laurentia and tectonic nappes were thrust SEwards onto the Baltic shield and formed the Bergen Arc System (e.g., Andersen et al. 1991; Fossen and Dunlap 1998; Jakob et al. 2017). The generated sequence is characterized

by different thrust sheets collected around Bergen and a crystalline basement of middle Proterozoic orthogneisses mainly composed of anorthositic granulites, jotunites, mangarites, and metagabbros (e.g., Austrheim and Griffin 1985). The deformation history of these rocks is coupled with a Caledonian eclogite-to-amphibolite-facies metamorphic overprint (e.g., Austrheim 1987) around  $\sim 430 \pm 3.5$  Ma (see Glodny et al. 2008b) at P–T conditions of  $\sim 2$  GPa and  $\sim 700$  °C (e.g., Bhowany et al. 2018; Kühn et al. 2002).

The rocks analyzed in this study are part of the island of Holsnøy (Fig. 1b), where brittle deformation fractured the granulitic host rock at eclogite-facies P–T conditions (e.g., Austrheim 1987; Jamtveit et al. 1990). Fractures and seismic fault planes permitted aqueous fluids to infiltrate into the metastable dry granulite-facies anorthosites. To decipher the fluid source Matthey et al. (1994) investigated the C, N and Ar isotopic compositions of the infiltrated fluid and suggested that it derived from sediments undergoing devolatilization. Regarding to Andersen et al. (2012) and Jakob et al. (2019) the sedimentary fluids have been released during the Caledonian orogeny and probably triggered the formation of the eclogite-facies shear zones. During metamorphism, the newly forming eclogite was mechanically weaker than the surrounding granulite and, thus more susceptible to accommodate ductile deformation (e.g., Jamtveit et al. 2018a, b; Jolivet et al. 2005; Petley-Ragan et al. 2018). This mechanism led to an extremely heterogeneous distribution of eclogite abundance (e.g., Austrheim 1987; Boundy et al. 1992; Schmid et al. 1998) resulting in different domains ranging from unaltered granulites and almost undeformed, minor eclogitized regions to areas of extensive eclogitization, which are highly deformed (Fig. 1b, e.g., Raimbourg et al. 2005; Zertani et al. 2019). Due to ongoing fluid infiltration, eclogitization, and deformation the eclogite-facies shear zones evolve from initial single veins to an interconnected shear zone network varying in width from millimeter to kilometer (Fig. 1c, e.g., Boundy et al. 1992, 1997; Fountain et al. 1994; Jolivet et al. 2005; Zertani et al. 2019). The hydrous and temporarily weak eclogite-facies shear zones widen during progressive deformation and fluid infiltration (e.g., Austrheim and Griffin 1985). Recently, Kaatz et al. (2021) showed that either a significant amount of fluid and/or numerous repetitive fluid pulses were necessary to recharge the shear zones and to enable shear zone widening during progressive deformation. While previous work has provided detailed information on how the eclogite-facies shear zones widen and interconnect during ongoing hydration and deformation, the mechanisms for incipient hydration are largely unknown.

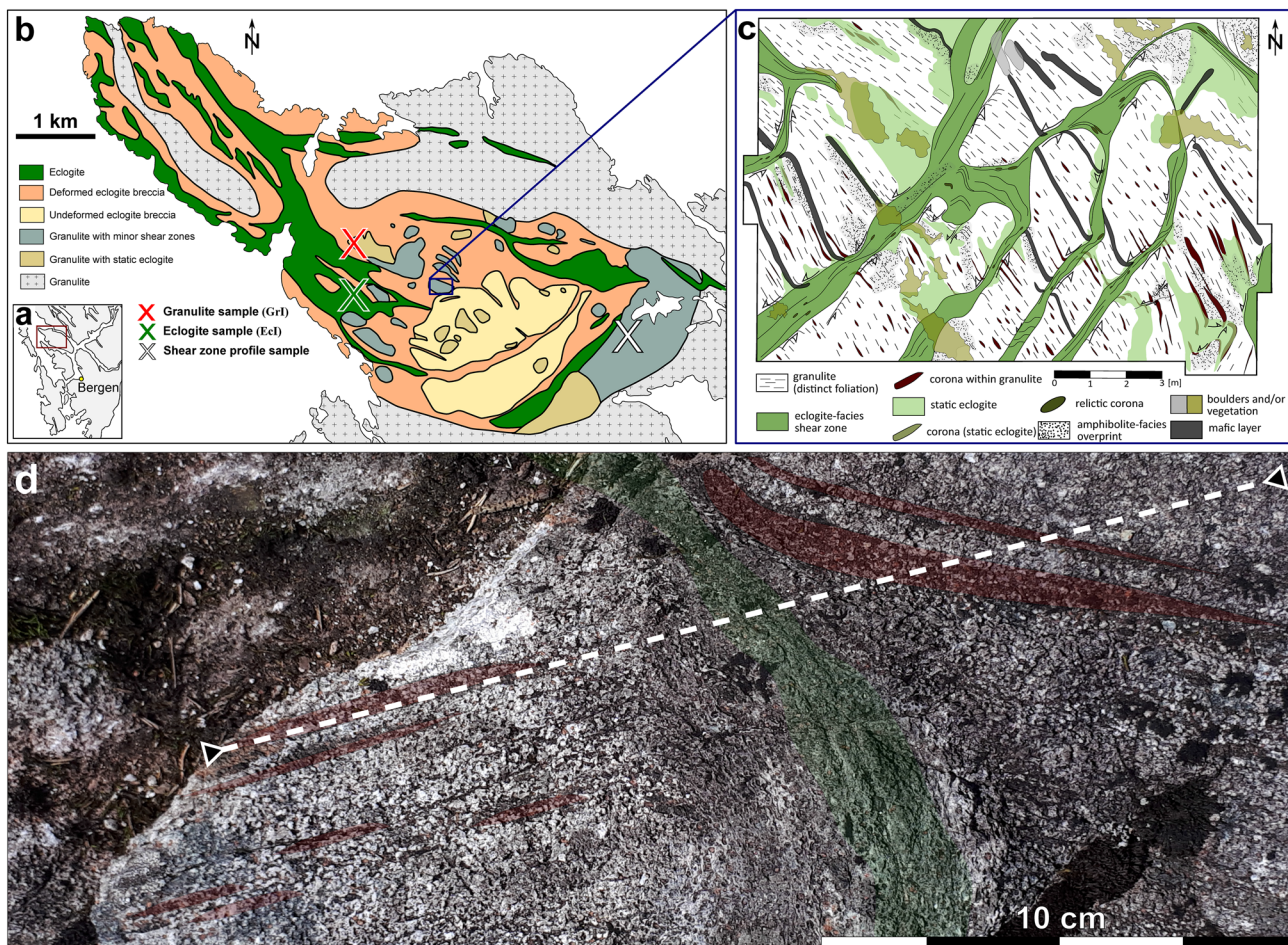


**Fig. 1** **b** Geological map of northwestern Holsnøy (Zertani et al. 2020, kilometer-scale) with an inset **a** showing the location of Holsnøy northwest of Bergen, Norway (red box). **c** Detailed outcrop map indicating the eclogite-facies shear zone network in areas mainly composed of granulite with minor shear zones (Kaatz et al. 2021, meter-

scale). **d** Field picture of the analyzed centimeter-wide eclogite-facies shear zone (highlighted in green) and the surrounding granulite (elongated coronas define the granulite foliation, red). The white dashed line indicates the profile line

## Macroscopic sample description

Within the scope of this study, an endmember sample of an unaffected granulite and a fully transformed eclogite as well as a cross-section through an incipient eclogite-facies shear zone were investigated. The unaltered granulitic host rock (GrI) was sampled in a pristine granulitic rock body north of a major eclogite-facies shear zone. The fully recrystallized eclogite (EcI) was taken from the center of the same major shear zone (see Fig. 1b for sample locations). The third sample is a 21.4 cm long section (Fig. 1d) crosscutting a small, cm-wide single shear zone at incipient eclogitization, which allows an accurate analysis of the mineral paragenesis during shear zone formation. The cross-section profile is subdivided into seven successive thick sections to guarantee continuous analysis of the mineral assemblage and textures.

## Analytical techniques

### Electron microprobe and scanning electron microscopy

Major element composition profiles for garnet, pyroxene and plagioclase grains were acquired on doubly polished thick sections (~240  $\mu\text{m}$ ) using a JEOL JXA 8800 SuperProbe electron microprobe microanalyzer (EMPA) at the Institute of Geological Sciences, Freie Universität Berlin. An accelerating voltage of 15 kV was used, with a beam current of 20 nA and a beam diameter of 1  $\mu\text{m}$ . For each element both peak and background were measured for 20 s, except for Ti and Na with 60 s/30 s, and 10 s/10 s, respectively. The number of spots for every transect may vary depending on the grain size as well as the density of fractures and inclusions. The general step size is 40–50  $\mu\text{m}$ . Structural formulae were

calculated based on 6, 8, 12 and 12.5 oxygens for clinopyroxene, plagioclase garnet and clinozoisite respectively.

Additionally, a Zeiss® Sigma 300 VP Field-Emission scanning electron microscope (SEM) of the Institute of Geological Sciences, Freie Universität Berlin, has been used to investigate different textures and mineral assemblages of the samples. The SEM is coupled to the Zeiss® Mineralogic system to conduct automated mineralogy using fully quantitative energy-dispersive spectroscopy (EDS) performed by Quantax Xflash 60mm<sup>2</sup> SSD. An accelerating voltage of 20 kV and a working distance of 9 mm was used to cover the entire thick sections.

### Fourier transform infrared spectroscopy (FTIR)

FTIR spectroscopy measurements were carried out on a Bruker® Tensor II FTIR system at the Institute of Geological Sciences of the University of Bern. This instrument is coupled with a Hyperion 3000 microscope, a liquid nitrogen cooled mercury cadmium telluride (MCT) detector and is equipped with a Plexiglas sample chamber with controlled air flow to limit H<sub>2</sub>O and CO<sub>2</sub> variations. Infrared spectroscopy uses the property of OH groups to vibrate (stretching) when exposed to specific frequencies of the mid-infrared light (3000–4000 cm<sup>-1</sup>). Frequencies of absorption are mineral, and defect specific. Typical OH-stretching band frequencies for garnet are in the range of 3650–3400 cm<sup>-1</sup> (e.g., Aines and Rossman 1984a), for clinopyroxene at 3650–3300 cm<sup>-1</sup> (Skogby et al. 1990) and at 3300–3200 cm<sup>-1</sup> for plagioclase (e.g., Johnson 2006). Doubly polished sample sections of ~240 µm thickness were used for transmission measurements. The samples were only polished down to 6 µm grit size to avoid signal interferences due to reflection, which may appear when the sample is polished down to 1 µm. Subsequently, all sample surfaces were glued back on a glass slide and repolished down to 1 µm for EMPA in order to correlate chemical composition and water content of the measured grain transects. The same transects were carefully analyzed with both methods, EMPA and FTIR. FTIR single spot analyses were obtained with the MCT detector, a 50 × 50 µm aperture size, a resolution of 8 cm<sup>-1</sup> and 64 scans.

### FTIR data processing

An atmospheric compensation and a baseline correction with 64 baseline points and four iterations was applied for all spectra using the concave rubber band algorithm in the OPUS® 7.5 software. Afterwards, distinct bands were defined to evaluate the OH absorbance area by integrating the area below the OH-stretching band, which is specific to each mineral. For the pyrope–almandine-rich garnet, the region 3620–3500 cm<sup>-1</sup> was considered, and the region

3730–3100 cm<sup>-1</sup> was monitored for the clinopyroxene (diopside–augitic composition and omphacite). As the plagioclase spectrum contains only one main band at 3200 cm<sup>-1</sup> but is partially affected by clinozoisite needles, the absorbance areas were calculated with MATLAB® via spectral deconvolution (Reynes et al. 2018). The deconvolution routine decomposes the signal (made of overlapping peaks) into single Lorentzian peaks and gives absorption area, height, width, and wavenumber position (see an example of a superposed spectrum for granulitic plagioclase and clinozoisite in supplementary material S1).

All single spot spectra were integrated with the B integration method of OPUS®. The water content (*wc*) is given in µg H<sub>2</sub>O per g of mineral and is linearly proportional to the total absorbance (*TotAbs*) following the Beer–Lambert law.

$$wc = TotAbs \times k_{abs}; \text{ with } k_{abs} = \frac{c \times M_{H_2O}}{d \times \epsilon} \quad (1)$$

The absorption coefficient ( $k_{abs}$  in cm<sup>2</sup>) is mineral specific and based on a constant  $c$  (10<sup>6</sup>) for conversion from µg to g, the molar mass of H<sub>2</sub>O ( $M_{H_2O}$ ), the mineral density  $d$ , and a calibration coefficient  $\epsilon$  (1 mol<sup>-1</sup> cm<sup>-2</sup>) determined for a specific mineral by an independent method. For garnets the calibration coefficient of Bell et al. (1995) for pyrope of 6700 l mol<sup>-1</sup> cm<sup>-2</sup> was used. For pyroxene, the coefficient of 83,400 l mol<sup>-1</sup> cm<sup>-2</sup> from Katayama et al. (2006) was used. To avoid overestimation of the calculated water contents this coefficient was used for omphacite as well because it leads to conservative estimates, as it is the highest coefficient provided in the literature for clinopyroxene (Bell et al. 1995; Katayama et al. 2006). The calibration coefficient for plagioclase is given by Johnson and Rossman (2003), 10,700 l mol<sup>-1</sup> cm<sup>-2</sup>. As the measurements were done using unpolarized light, an average H<sub>2</sub>O content for pyroxene and plagioclase is computed by firstly calculating an average absorbance on multiple randomly oriented grains and then multiplying this measured average total absorbance by three (e.g., Kovács et al. 2010).

## Results

### Detailed sample description

The granulite endmember sample (GrI, host rock) has a weak lineation defined by flattened coronas, which consist of clinopyroxene (pyx, diopside to augitic composition, Table 1) surrounded and mixed with garnet (grt) of homogeneous composition (~Alm<sub>28</sub>Pyr<sub>54</sub>Grs<sub>18</sub>). The sample is coarse grained (1–3 mm) and consists of 70 vol.% of granulitic plagioclase (~An<sub>45</sub>Ab<sub>54</sub>). Plagioclase (plg) grain

**Table 1** Representative mineral chemical data of garnet (granulitic core and eclogite-facies rim), clinopyroxene (granulitic pyroxene and omphacite), granulitic plagioclase, and clinozoisite (Zone I, III, and

EcI) for the analyzed samples (in wt.%). Structural formulae were calculated on the basis of 12, 6, 8, and 12.5 oxygens, respectively

	grt core	grt rim	Granulitic pyx	omph		Granulitic plg	czs EcI	czs Zone III	czs Zone I
SiO <sub>2</sub>	41.09	39.67	47.30	55.03		56.58	39.42	39.33	41.08
TiO <sub>2</sub>	0.12	0.06	1.06	0.20		0.03	0.03	0.04	0.05
Al <sub>2</sub> O <sub>3</sub>	22.30	21.55	11.86	12.81		27.43	31.94	31.88	32.28
Fe <sub>2</sub> O <sub>3</sub>	–	–	–	–		–	2.52	2.47	0.67
FeO	14.55	22.20	5.42	4.36		0.00	–	–	–
MgO	14.55	9.84	11.04	7.70		–	0.09	0.04	–
MnO	0.22	0.43	0.03	0.06		–	–	–	–
CaO	7.17	6.35	21.44	12.86		9.56	23.99	23.68	23.52
Na <sub>2</sub> O	–	–	1.79	7.00		6.16	0.01	0.03	–
K <sub>2</sub> O	–	–	–	–		0.20	–	–	–
<b>Σ</b>	<b>100.0</b>	<b>100.1</b>	<b>99.9</b>	<b>100.0</b>		<b>99.9</b>	<b>98.0</b>	<b>97.47</b>	<b>97.6</b>
Si	3.01	3.01	1.73	1.95		2.54	6.11	6.12	6.24
Ti	0.01	0.00	0.03	0.01		0.00	0.02	0.00	0.00
Al	1.93	1.93	0.51	0.54		1.45	5.84	5.85	5.78
Fe <sup>3+</sup>	0.04	0.05	0.10	0.03		–	0.22	0.20	0.19
Fe <sup>2+</sup>	0.85	1.36	0.06	0.10		–	0.02	0.02	0.02
Mg	1.59	1.11	0.60	0.41		–	0.02	0.01	–
Mn	0.01	0.03	0.00	0.00		–	–	–	–
Ca	0.56	0.52	0.84	0.49		0.46	3.97	3.95	3.83
Na	–	–	0.13	0.48		0.54	0.02	0.01	–
K	–	–	–	–		0.01	–	–	–
<b>Σ</b>	<b>8.0</b>	<b>8.0</b>	<b>4.0</b>	<b>4.0</b>		<b>5.0</b>	<b>16.2</b>	<b>16.1</b>	<b>16.0</b>
Pyr	52.7	36.9	Jd	2.3	An	44.8	45.6		
Alm	28.2	45.0	Ae	10.4	Ab	3.3	53.2		
Gro	18.3	16.7	WEF	87.3	Or	51.9	1.2		
Sps	0.4	0.9							
Uva	–	–							
And	0.4	0.5							

Note: Clinopyroxene nomenclature is given after Morimoto (1988), which includes the composition of magmatic relicts. Fe<sup>3+</sup> and Fe<sup>2+</sup> were recalculated using a fixed cation sum of 8 (grt) and 4 (pyx)

boundaries are occasionally surrounded by a few clinozoisite needles (czs, ~1 vol.%) due to the phase separation of granulitic plagioclase into symplectites consisting of an albite-rich plagioclase and clinozoisite during high-pressure metamorphism. The eclogite endmember (EcI) consists of a fine-grained (< 1 mm) matrix composed of garnet, omphacite (omph), phengite, clinozoisite, and accessory phases, e.g., quartz, kyanite, and amphibole (amph). A representative omphacite composition is given in (Table 1). The eclogite foliation is produced by the alignment of the matrix minerals. Garnet is highly fractured and has a core of the pristine granulite-facies composition (~ Alm<sub>28</sub>Pyr<sub>54</sub>Grs<sub>18</sub>) and an eclogite-facies, Fe-rich rim (~ Alm<sub>42</sub>Pyr<sub>37</sub>Grs<sub>21</sub>).

Figure 2a shows thick sections of one side of the cross-section sample from the mm-wide eclogite-facies shear zone (left part) towards the granulitic host rock (right part). The analyzed profile is oriented perpendicular to the shear zone

to examine the lateral distribution of H<sub>2</sub>O infiltration out of the shear zone.

Figure 2b displays how the phase abundances change along the profile. This was obtained by SEM phase map data of the thick sections. Due to changing phase abundances and microscopic textural characteristics, the profile can be separated into three different zones. Zone I is farthest away from the shear zone center (Fig. 2a, right side). This part represents the most pristine granulite and is less affected by fluid. This granulitic host rock is strongly foliated with elongated coronas as highlighted in (Fig. 1d). The outermost right part of Zone I is macroscopically characterized by the typical granulitic texture with coarse-grained (1–2 mm) granulitic plagioclase (~60 vol.%, ~An<sub>45</sub>Ab<sub>54</sub>) with distinct grain boundaries and very small amounts of clinozoisite (~1.5 vol.%, Fig. 2e). In lateral direction towards the shear zone the plagioclase grain boundaries start to vanish, and the

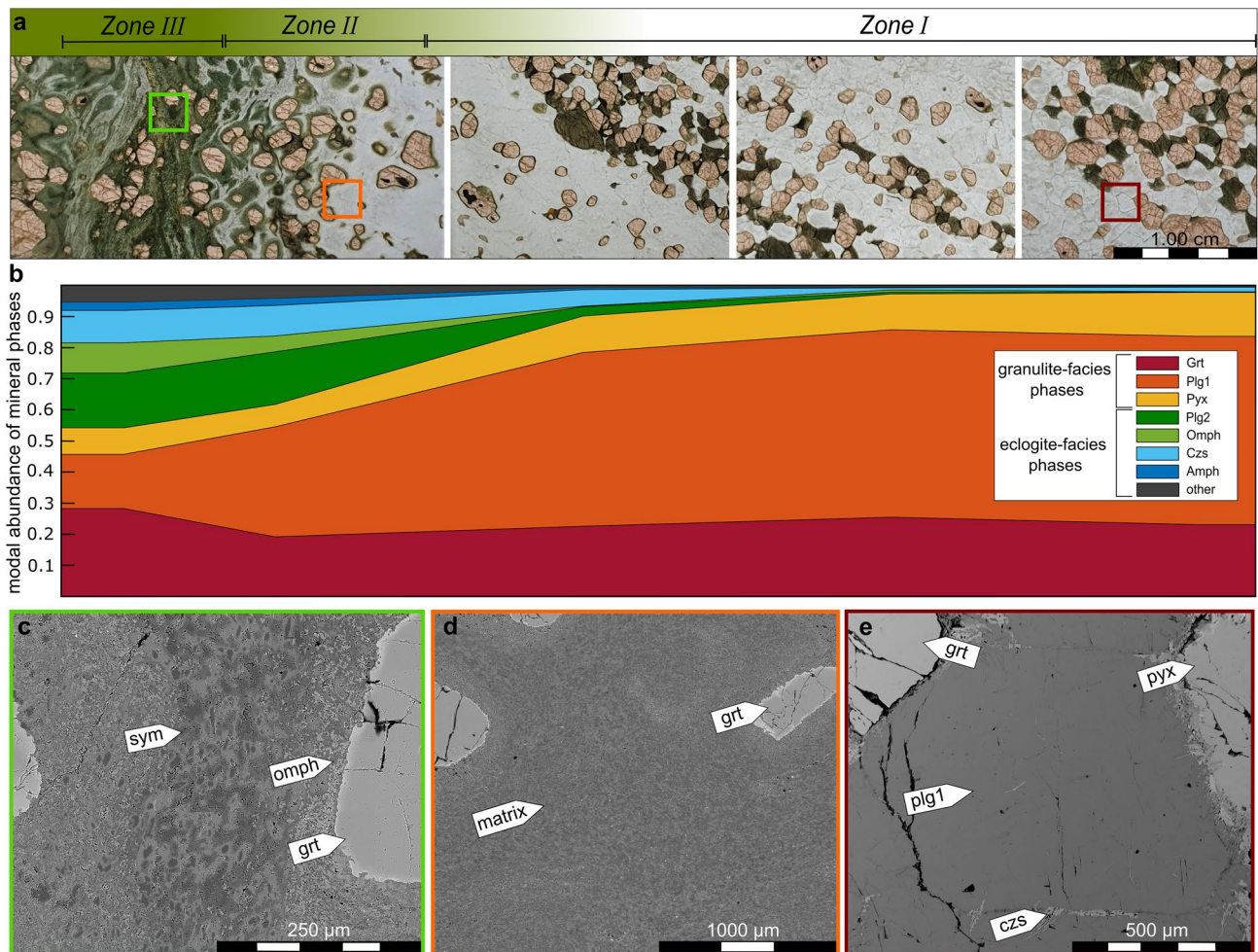


**Fig. 2** **a** Thick-section images of the analyzed profile. The top indicates the transition from granulite-facies (white, right side) to eclogite-facies mineral assemblage (green, left side), relating to the modal abundances of mineral phase (in vol.%) shown in **(b)**. The profile is subdivided into 3 different zones: Zone I, is furthest away from the eclogite-facies shear zone and characterized by distinct plagioclase grain boundaries and smaller amounts of clinozoisite; Zone II, is the shear zone rim, and the transition between granulite and eclogite; Zone III, is the mm-wide eclogite-facies shear zone composed of omphacite, garnet and higher amounts of czs and amphibole com-

pared to Zone I. **b** All granulite-facies phases are grouped to yellowish colors, including garnet (grt), granulitic plagioclase (plg1) and pyroxene (pyx). Eclogite-facies phases are grouped in green to blue colors, where green represents anhydrous phases, e.g., omphacite (omph) and albitic plagioclase (plg2), and blue illustrates hydrous phases, e.g., clinozoisite (czs) and amphibole (amph). Gray depicts minor phases, e.g., kyanite, phengite, quartz. Representative BSE photographs of Zone III **c**, Zone II **d** and Zone I **e** show the microstructural differences, e.g., grain-size reduction of plagioclase

entire plagioclase converts more and more into a symplectite made up of the albite-rich plagioclase and clinozoisite. This symplectite is pseudomorphically replacing the granulitic plagioclase. Therefore, the amount of clinozoisite (~5 vol.%) and of albite-rich plagioclase (~3 vol.%) increases towards the shear zone. Pyroxenes are homogenous in composition and constant in size. Zone II is defined as the outer rim of the shear zone. This part is characterized by a very fine-grained matrix (<50  $\mu$ m) mainly composed of granulitic plagioclase relicts (~35 vol.%), clinozoisite (~9 vol.%), albite-rich plagioclase (~16 vol.%), and omphacite (~5 vol.%), commonly accumulated around garnets (Fig. 2a). Almost no distinct

plagioclase grain boundaries are left, and individual single grains can hardly be identified (Fig. 2d). Some pristine pyroxene relicts are still present. Zone III is the eclogite-facies shear zone. The fine-grained matrix (~50  $\mu$ m) consists of omphacite (~9 vol.%), clinozoisite (~10 vol.%), albitic plagioclase (~17 vol.%), granulitic plagioclase relicts (~17 vol.%), and others including amphibole, phengite and kyanite. During metamorphic transformation the garnet rims become more irregular on a first glance but on a closer view an eclogite-facies rim forms indicating equilibrium conditions with its adjacent phases on the  $\mu$ m to tens of  $\mu$ m scale. The thickness of this rim increased towards the shear zone

from Zone I to Zone III (compare Fig. 2c, e). Additionally, the garnets are highly fractured due to brittle deformation.

Reaction progress from Zone I to Zone III is visible in the abundance of eclogite-facies phases and hydrous phases, as well as textural changes, e.g., significant reduction of the average grain size for plagioclase.

## Garnet

Thirty-five rim-to-core-to-rim transects were acquired, including samples GrI and EcI. Four representative transects are shown in the (Fig. 3a–d), where mineral chemistry profiles (EMPA data) are combined with the determined H<sub>2</sub>O content profiles (calculated from FTIR data). Garnet of Zone I (Fig. 3d) shows the typical homogenous granulitic composition of ~ Alm<sub>29</sub>Pyr<sub>52</sub>Grs<sub>19</sub> without any compositional variations. The grains shown in (Fig. 3a, b) are located within the shear zone (3a) and directly next to it (3b) showing the granulitic composition within the garnet core, whereas the composition of the outermost rim changes to eclogite-facies garnet composition of ~ Alm<sub>45</sub>Pyr<sub>36</sub>Grs<sub>19</sub>, on average (Table 1). The BSE images displayed in (Fig. 3a, d) show one representative garnet grain boundary of Zone III and Zone I, respectively. The bright eclogite-facies rim is present in all garnet grains but expanded in Zone III (3a) compared to Zone I (3d). The garnet rims are enriched in FeO compared to the garnet core and become more irregular towards the shear zone. The insets in (Fig. 3a, d) displays the shape of the garnet grain boundary and the surrounding,

newly formed omphacite grains. At high-spatial resolution the garnet grain boundaries of Zone III are regular, distinct, and partially form angles of 120° (Fig. 3a). The ones of Zone I are at all scales often regular and very sharp (Fig. 3d).

Representative spectra of granulite-facies garnet cores of Zone I (red), Zone III (light blue), and of the eclogite endmember sample EcI (violet) are shown in (Fig. 4a). Additionally, a typical spectrum of the eclogite-facies garnet rims, Zone III, is given in dark blue. The shape of all garnet spectra is characterized by a prominent broad absorption band around 3565 cm<sup>-1</sup>. The eclogite-facies garnet rim from Zone III has an additional band at 3650 cm<sup>-1</sup>. Transects of H<sub>2</sub>O contents through garnet grains reveal that the granulite-facies cores display a plateau whereas the eclogite-facies rim concentrations are higher (Fig. 3). The H<sub>2</sub>O contents in the cores of the garnet furthest away from the shear zone (Fig. 3d) are the lowest and constantly between 5 and 10 µg/g. On average, the water contents of the granulite-facies garnet cores moderately increase from Zone I to Zone III up to ~ 50 µg/g (Fig. 3a). Especially in Zone II and III the H<sub>2</sub>O content increases towards the garnet rim still within the parts characterized by the granulite-facies composition (Fig. 3b), but also within the eclogite-facies garnet rim (Fig. 3a). The garnet rims partially have about three times more H<sub>2</sub>O than determined for the granulitic garnet cores within 200 µm distance and independent of any other possible compositional changes (Fig. 3a, b). This bowl-shape water profile is characteristic for garnet. No constant H<sub>2</sub>O plateau values were detected for the eclogite endmember

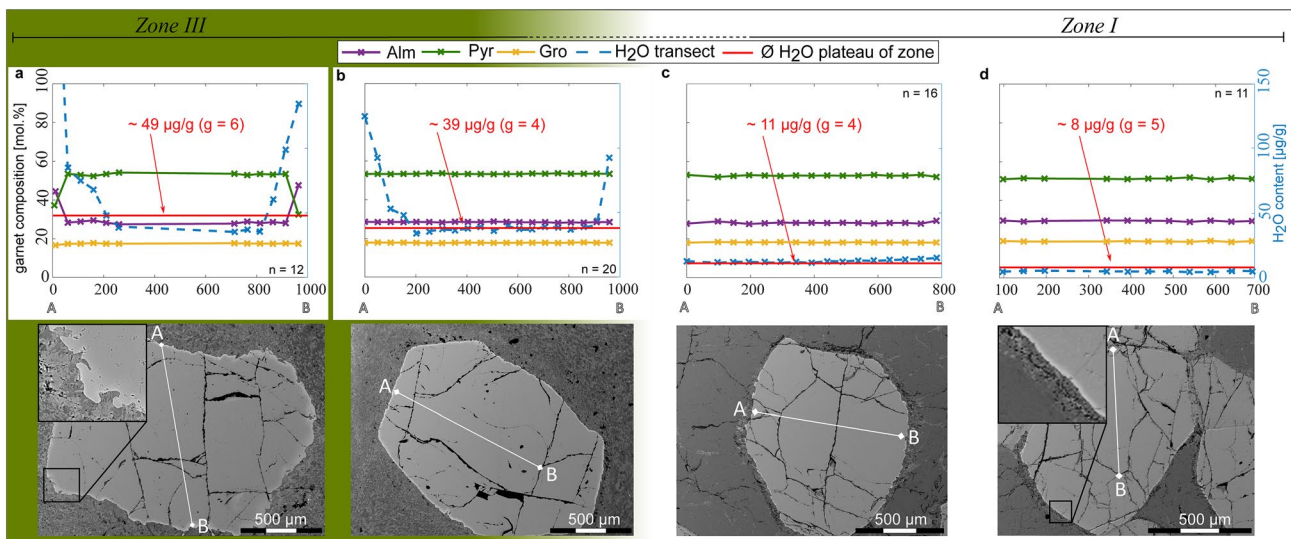
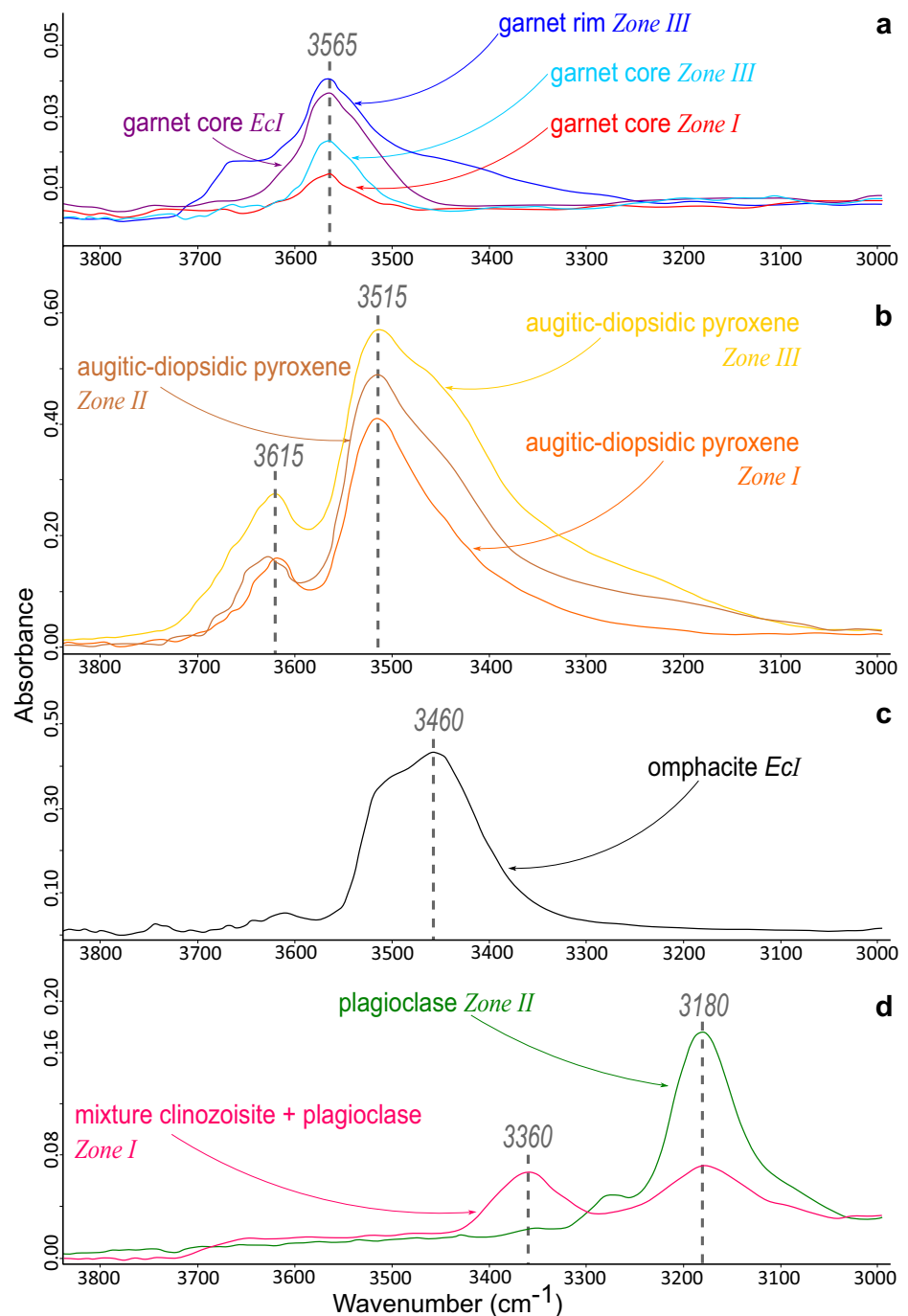


**Fig. 3** Representative garnet composition transects with H<sub>2</sub>O content profiles and the average plateau water contents of each zone. BSE images are given for the associated grains. **a** Zone III, **b** Zone II, **c**, **d** are parts of Zone I with increasing distance to eclogite-facies shear zone, respectively. Plots have an x-axis showing the transect length in µm, left y-axis indicates the endmember compositions (in mol. %),

and the right y-axis the H<sub>2</sub>O content (in µg/g). Abbreviations used: *Alm* almandine, *Pyr* pyrope, *Gro* grossular, *H<sub>2</sub>O* water content, *n* datapoints of one transect, and *g* number of measured grains. Insets in **a**, **d** highlight the increasing irregularity of the garnet rims with decreasing distance to the eclogite-facies shear zone

**Fig. 4** Single representative IR absorption spectra for **a** garnet cores and rim of Zone I, Zone III and sample EcI with a main OH-stretching band around  $3565\text{ cm}^{-1}$ ; **b** IR spectra of the granulitic pyroxenes of Zone I–III with two OH-stretching bands around  $\sim 3515\text{ cm}^{-1}$  and  $\sim 3615\text{ cm}^{-1}$ ; **c** Omphacite spectra with its characteristic OH band at  $3460\text{ cm}^{-1}$ ; **d** Plagioclase of Zone II with a main OH band occurring between  $3180$  and  $3210\text{ cm}^{-1}$ , and a mixed spectra of plagioclase and clinzoisite ( $\sim 3360\text{ cm}^{-1}$ ) of Zone I



sample (EcI), probably due to the high number of cracks observed in this sample. The EcI sample is highly deformed and garnet cores are partly fractured, which affects the water supply into the grain core causing  $\text{H}_2\text{O}$  values ranging from 25 to  $85\text{ }\mu\text{g/g}$  (9 grains). The garnet cores of sample GrI show  $\text{H}_2\text{O}$  contents varying between 10 and  $25\text{ }\mu\text{g/g}$  (5 grains), resembling the values of Zone I of the shear zone profile. These  $\text{H}_2\text{O}$  contents are similar to what has been reported in granulite garnets by Malvoisin et al. (2020).

### Clinopyroxene

For the granulitic pyroxene, 23 suitable transects have been measured, including sample GrI. The pyroxene has a diopsidic to augitic composition with  $\text{Jd}_1\text{--Jd}_5$ . The granulitic pyroxene composition remains constant except for a small increase in the average jadeite component ( $\text{NaAlSi}_2\text{O}_6$ ) and in aluminum beside a slight decrease of the  $\text{NaFe}_3\text{Si}_2\text{O}_6$



component from Zone I to III (Table 2). Altogether, the sample GrI and EcI fit this trend.

Three pyroxene IR spectra are shown in (Fig. 4b) with the strongest absorption at  $\sim 3515\text{ cm}^{-1}$ , which is very similar to one main band described for diopside (e.g., Skogby et al. 1990). Additionally, all granulitic pyroxenes display a second and lower band around  $3615\text{ cm}^{-1}$ , which increases with decreasing distance to the eclogite-facies shear zone. Moreover, pyroxene spectra of Zone II and III exhibit a shoulder around  $3460\text{ cm}^{-1}$ . This was not observed for pyroxenes in Zone I or GrI. Figure 5a–d shows representative  $\text{H}_2\text{O}$  contents and mineral chemistry profiles of four single pyroxene grains. Almost every grain shows a  $\text{H}_2\text{O}$  increase from the core towards the rims, as shown in (Fig. 5c) (Zone I). Mostly all pyroxene grains display this bowl-shape type water profiles. Although, the rise is not as steep in all grains, almost every grain shows a  $\text{H}_2\text{O}$  plateau around the lowermost values within the grain core. The  $\text{H}_2\text{O}$  concentration of pyroxene in each zone was calculated from pooling the absorption

values of the cores in each zone together to account for differences in absorbance due to different orientations of the pyroxenes. Subsequently, the average of these absorption values was multiplied by 3 to obtain the total absorbance (Kovács et al. 2010). The  $\text{H}_2\text{O}$  concentrations within the pyroxene cores increase from Zone I, on average  $140\text{ }\mu\text{g/g}$ , to Zone III, approximately  $310\text{ }\mu\text{g/g}$ . One pyroxene grain of the GrI displays the lowest water contents for pyroxene of  $\sim 50\text{ }\mu\text{g/g}$ , but the average plateau  $\text{H}_2\text{O}$  content for the GrI pyroxenes is  $\sim 100\text{ }\mu\text{g/g}$ .

Newly formed omphacite grains within the eclogite-facies shear zone center are too small to be analyzed in detail. Therefore, 12 omphacite transects of the EcI sample were investigated. The composition of omphacite ranges from  $\text{Jd}_{41}$  to  $\text{Jd}_{47}$ .

One representative IR spectrum of the omphacite is given in Fig. 4c and displays two bands between  $3400$  and  $3550\text{ cm}^{-1}$  with the strongest absorption at  $3460\text{ cm}^{-1}$ . Occasionally, omphacite has a third band at  $3630\text{ cm}^{-1}$  (e.g.,

**Table 2** Jadeite and Ca-Tschermakite endmembers calculated for clinopyroxene using Cawthorn and Collerson (1974) for  $n$  data points and each zone, including the endmember samples

Area	OH ( $\mu\text{g/g H}_2\text{O}$ )	$\text{NaAlSi}_2\text{O}_6$	Na (apfu)	$\text{CaAlAlSiO}_6$	Al (apfu)	$\text{NaFe}_3\text{Si}_2\text{O}_6$	$n$
GrI	65	0.031	0.122	0.209	0.510	0.092	62
Zone I	140	0.013	0.117	0.205	0.457	0.113	123
Zone II	200	0.021	0.113	0.200	0.467	0.108	44
Zone III	310	0.068	0.129	0.171	0.462	0.068	26
EcI (omph)	230	0.443	0.469	0.033	0.522	0.026	108

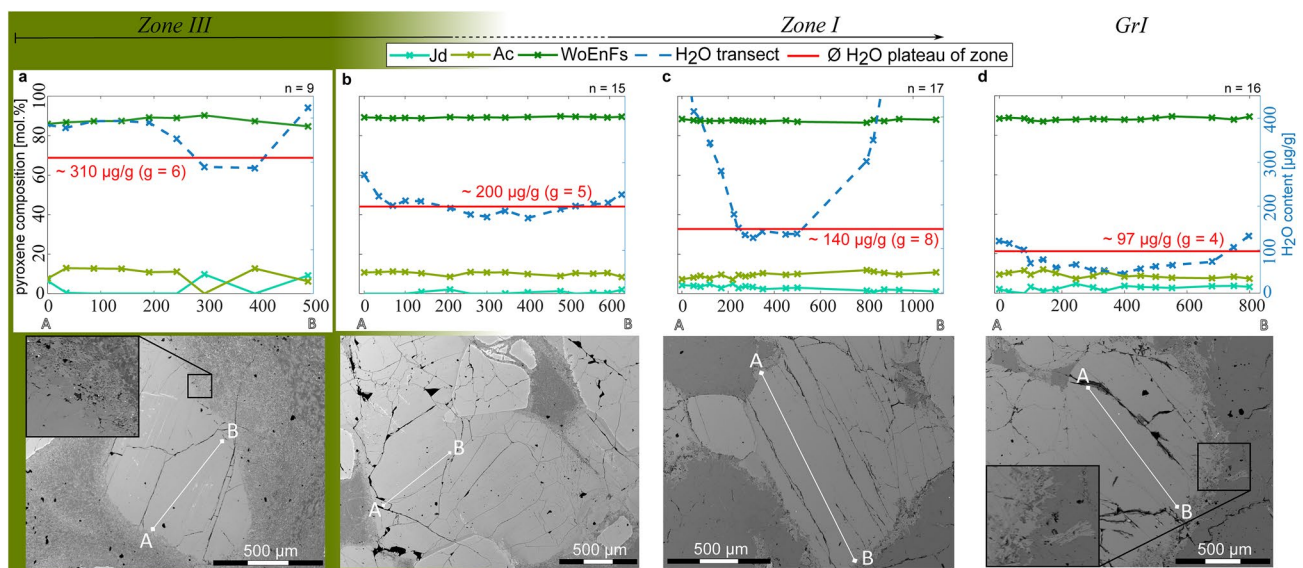


**Fig. 5** Representative  $\text{H}_2\text{O}$  content and mineral composition profiles of single pyroxene grains from Zone III (a), Zone I (b, c), and sample GrI (d). X-axis showing the transect length in  $\mu\text{m}$ , left y-axis displays the endmember compositions (in mol. %), and right y-axis the  $\text{H}_2\text{O}$  content up to  $450\text{ }\mu\text{g/g}$ . Abbreviations for endmembers: *Jd* jadeite, *Ac* actinomite, *WoEnFs* wollastonite/enstatite/ferrosilite, *H<sub>2</sub>O* water content,

$n$  datapoints of one transect, and  $g$  number of measured grains. BSE images show the associated pyroxene grains and insets in a, d demonstrate that amphibole, phengite and clinozoisite are likely to form directly at pyroxene grain boundaries, commonly where in contact with plagioclase

Skogby 2006), which is almost negligible to absent in the analyzed omphacites. Contrary to the granulitic pyroxene, in most of the omphacite transects the H<sub>2</sub>O content either slightly decreases towards the rim or water contents are approximately constant within one grain (Fig. 6). Omphacite shows H<sub>2</sub>O contents from 150 µg/g to 425 µg/g.

## Plagioclase

The granulite-facies plagioclases of Zone I and the granulite endmember sample GrI have in general a composition of An<sub>45</sub>Ab<sub>54</sub>Or<sub>1</sub> (Table 1, Fig. 7a, b). During the metamorphic rock transformation, the granulitic plagioclase underwent an almost isochemically (only H<sub>2</sub>O has been added) phase separation forming symplectites (Wayte et al. 1989) consisting of clinozoisite and a more albite-rich plagioclase (~An<sub>28</sub>Ab<sub>71</sub>). The plagioclase grains of the outermost part of Zone I appear very clean with rare clinozoisite needles (1–2 mm) mostly at their grain boundaries (Fig. 7a). With decreasing distance to the shear zone, the former granulitic plagioclase (~An<sub>45</sub>Ab<sub>54</sub>) converts into a fine-grained matrix, ~50 µm on average (Fig. 7c, d), consisting of granulitic plagioclase relicts and symplectites (czs + albitic plagioclase, ~An<sub>28</sub>Ab<sub>71</sub>). In Zone III, less pristine plagioclase grains are left (Fig. 7e). The clinozoisite needles change their composition and have higher iron contents with decreasing distance to the shear zone (Table 1).

IR spectra of the granulite-facies plagioclase display a characteristic OH-stretching band between 3180 and

3210 cm<sup>-1</sup> (Fig. 4d). Additionally, almost all plagioclases show a shoulder around 3280 cm<sup>-1</sup>. Towards the eclogite-facies shear zone, this minor band vanishes. One result of phase separation is the increasing volume of clinozoisite needles. The characteristic OH absorbance of clinozoisite superposes the plagioclase spectra (Fig. 4d). The OH-stretching band for clinozoisite is at 3360 cm<sup>-1</sup>. Both OH bands were differentiated by deconvolution (method described in Reynes et al. 2018). The water contents of the granulitic plagioclase increase from Zone I towards the shear zone from, ~10 µg/g up to a maximum of ~144 µg/g and the water profiles are usually flat. Due to the phase separation Zone II is the area closest to the eclogite-facies shear zone where water can be measured in the plagioclase grains by minimizing the possibility that the measurements reflect a mixture of both plagioclases, the precursor high-An plagioclase and the newly formed high-Ab plagioclase. The average water content detected here is approximately ~74 µg/g, with some few maximum values around 140 µg/g.

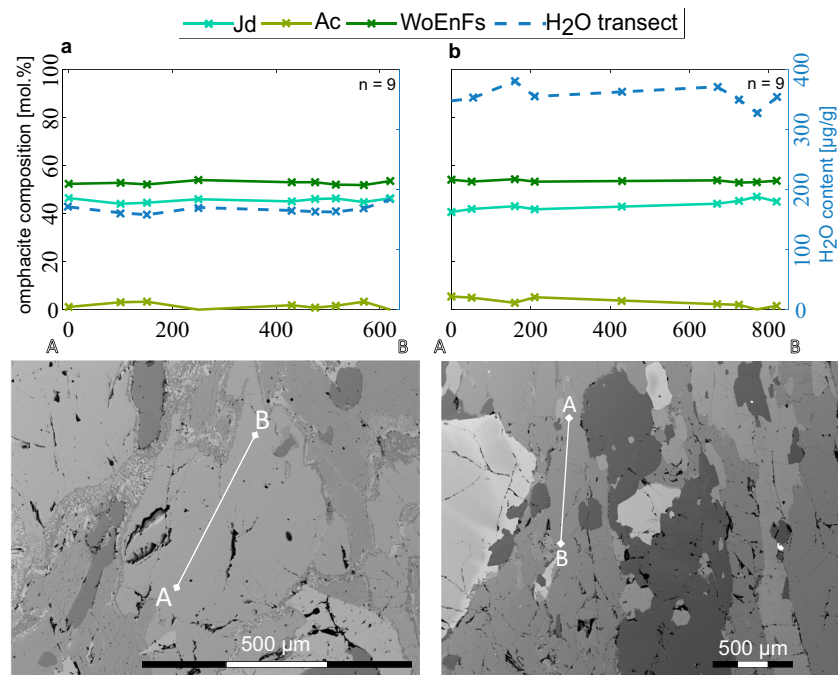
## Discussion

### OH incorporation in nominally anhydrous minerals

#### Garnet

The spectra of both granulitic garnet core and eclogite-facies garnet rim have a single band around 3565 cm<sup>-1</sup>.

**Fig. 6** Mineral composition and H<sub>2</sub>O content profiles of two representative omphacite grains of sample Ecl. X-axis shows the length of the transect (µm); left y-axis displays the lateral endmember compositional variations of omphacite (in mol. %); and the right y-axis the H<sub>2</sub>O content (in µg/g). **a** Is an omphacite grain with the lowest water contents detected (~150 µg/g), and **b** is a grain with one of the highest water contents (~350 µg/g). Abbreviations as described in Fig. 5



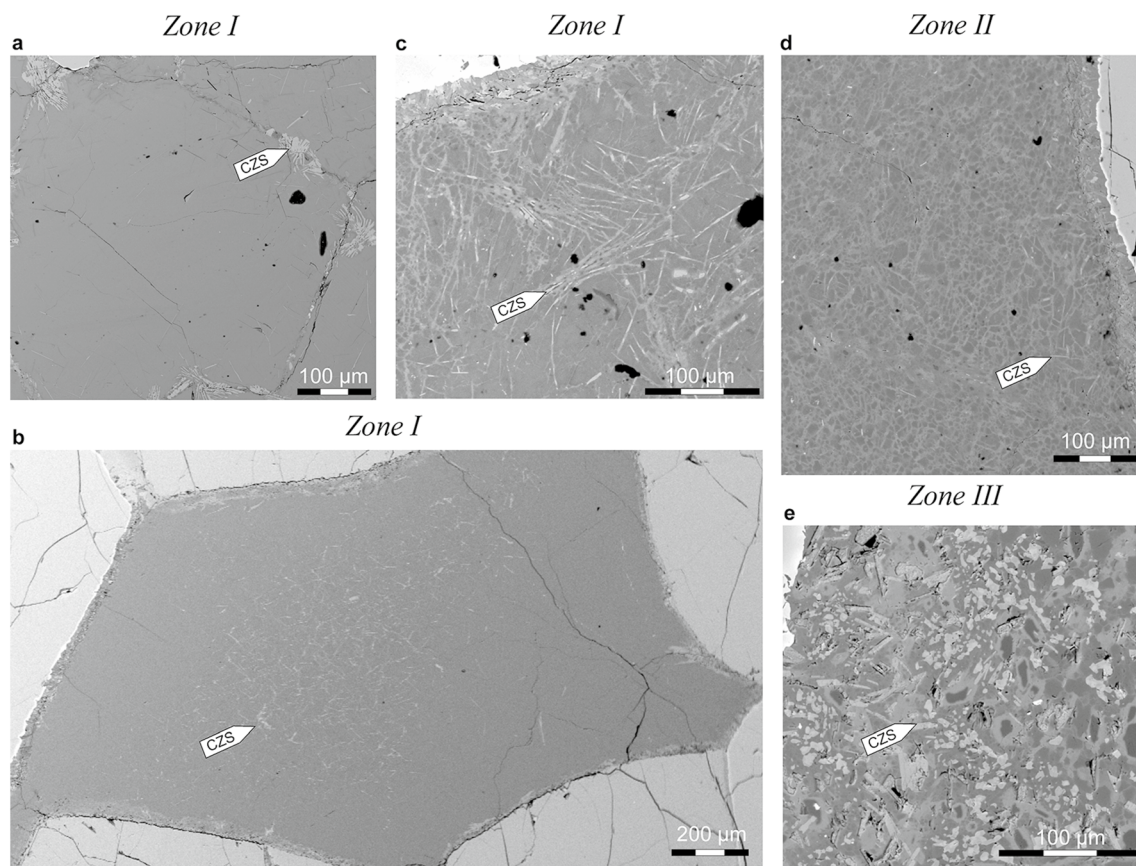


**Fig. 7** BSE images are shown to compare plagioclase characteristics of Zone I to Zone III. At the outermost part of Zone I **a, b** the plagioclase is almost unaltered with much less clinozoisite. The clinozoisite mainly occurs at the plagioclase grain boundaries but also inside the

plagioclase core. In Zone I **c** nearer to the shear zone and Zone II **d** phase separation is visible throughout the entire plagioclase grain. As a result of ongoing phase separation almost no granulitic plagioclase is left in Zone III **e**, and the matrix average grain size is reduced

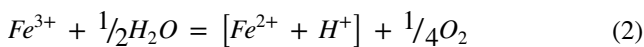
There is no shift in the OH-stretching band even though the garnet composition changes from  $\sim \text{Alm}_{28}\text{Pyr}_{53}\text{Grs}_{18}$  to  $\sim \text{Alm}_{45}\text{Pyr}_{37}\text{Grs}_{17}$ . The most widely recognized point defect for OH incorporation in garnet is the hydrogarnet substitution where  $\text{Si}^{4+}$  is replaced by  $4\text{H}^{+}$  in the tetrahedral site (e.g., Cohen-Addad et al. 1967). This defect produces a different IR-band depending on the garnet composition (Aines and Rossman 1984b). In the measured garnet, the OH band is neither characteristic of pure pyrope ( $3623\text{ cm}^{-1}$ , e.g., Geiger et al. 1991) nor for almandine ( $3550\text{ cm}^{-1}$ , e.g., Aines and Rossman 1984a). The broad OH band, between the two OH band positions, might suggest a solid-solution of the endmembers causing an intermediate band position at  $3565\text{ cm}^{-1}$ . The observed spectra are similar to mantle garnets having a band at  $3570\text{ cm}^{-1}$  (e.g., Aines and Rossman 1984b; Bell and Rossman 1992), which are usually pyrope-almandine solid solutions with a minor grossular content. A second hypothesis is that the absorption is related to an andradite ( $\text{CaFe}^{3+}$ ) component in garnet (Amthauer and Rossman 1998; Geiger and Rossman 2020), which shows a single peak at  $3565\text{ cm}^{-1}$ . The microprobe analysis (Table 1)

reveals a minor andradite component in the analyzed garnets ( $< 1\text{ mol.}\%$ ), which might be enough to explain incorporation of OH in such a micro-environment. The observation that there is no shift in absorption bands from granulite to eclogite-facies garnet despite major element composition shift supports this second hypothesis.

The  $\text{H}_2\text{O}$  contents of the eclogite-facies garnet are generally up to 30 times higher ( $> 150\text{ }\mu\text{g/g}$ ) than the  $\text{H}_2\text{O}$  contents of the granulite-facies garnet ( $\sim 10\text{ }\mu\text{g/g}$ ). The newly formed eclogite-facies garnet rims grew in the presence of a free fluid phase (e.g., Raimbourg et al. 2007), and thus likely represent the equilibrium value for this composition at the given P–T conditions. The water contents of the granulite-facies garnets are more intriguing. They show two main features. Firstly, the concentrations of  $\text{H}_2\text{O}$  in the core increase from Zone I ( $5\text{--}10\text{ }\mu\text{g/g}$ ) to Zone III ( $50\text{ }\mu\text{g/g}$ ) by a factor of five to ten, while major element concentrations remain the same. Secondly, transects through single grains show a plateau  $\text{H}_2\text{O}$  content in the core and then a pronounced increase towards the rim. Both features occur in the granulitic garnet composition (Fig. 3b) and hence, are not related

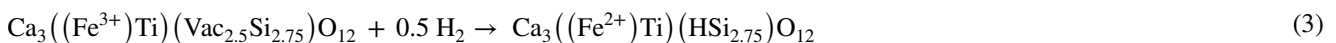
to recrystallization. Instead, these features are characteristic of diffusive processes that must have occurred during the fluid influx into the previously dry granulite. The H<sub>2</sub>O content increase from core to rim provides strong evidence that no modification of the H<sub>2</sub>O occurred during exhumation of the rocks, as this would result in decreasing H<sub>2</sub>O contents from core to rim. Therefore, the observed increase of H<sub>2</sub>O contents in the granulitic garnets is interpreted to relate to diffusive H<sub>2</sub>O intake during the formation of the hydrous eclogite-facies shear zone. To obtain a plateau concentration of H<sub>2</sub>O contents, fast diffusion is required.

Reynes et al. (2018) have revealed that the fastest H diffusion (out) mechanism in garnet is likely related to iron oxidation. The reverse mechanism might enable a fast hydration mechanism, with reduction of a Fe<sup>3+</sup> into Fe<sup>2+</sup> charge balanced by the incorporation of H as described by the following generalized equation:



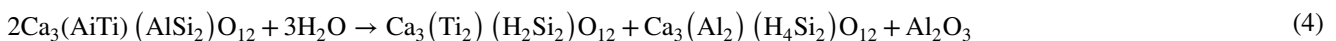
The available amount of Fe<sup>3+</sup> in the granulite-facies garnet places then an upper limit of how much hydrogen can be incorporated with this mechanism. This “proton–polaron” exchange (Mackwell and Kohlstedt 1990) is orders of magnitude faster than vacancy or cation diffusion in silicates (Jollands et al. 2021) and able to “decorate” pre-existing defects with hydrogen. In H decoration experiments of olivine, Tollan et al. (2018) observed similar shaped profiles as found in the garnets here, with a plateau H<sub>2</sub>O concentration in the cores and a small rim with increased H<sub>2</sub>O. They could show that plateau concentrations were related to a fast proton–polaron reaction, while the increase in the rims was probably related to H<sub>2</sub>O incorporation due to metal vacancy diffusion. Therefore, the assumption is that the H<sub>2</sub>O increase towards the rims is governed in a similar way by a slower diffusion mechanism that involves metal vacancies. The two different hydration processes for the analyzed garnet can be described by the following equations:

Fast hydrogen proton diffusion



which corresponds to 1/4 of a hydrogrossular substitution.

Slower diffusion involving also movement of hydrogen associated to cation vacancies



In a different eclogite-facies shear zone in the Holsnøy granulite, Malvoisin et al. (2020) observed granulitic garnets with higher H<sub>2</sub>O contents of 150 µg/g in the core and ~ 50 µg/g in the rims. The particular zoning of

the garnet was interpreted as decoration of pre-existing defects in garnet during a fluid influx event, followed by diffusional loss and recrystallization of minerals around garnet immediately after the H uptake. It is interesting to note that the rim H<sub>2</sub>O contents of Malvoisin et al. (2020) approximately correspond to the plateau concentrations of garnet within the eclogite-facies shear zone analyzed in this study.

### Clinopyroxene

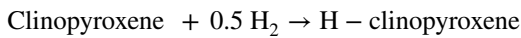
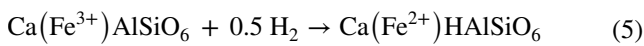
The analyzed granulitic pyroxene shows diopsidic to augitic compositions. Recently Balan et al. (2020) indicated that diopside mainly shows three different OH-bearing defects at the T-, M2-, or M1-site of the crystal lattice. Among the most common substitutions H-substitutions are associated to trivalent cations (e.g., Ingrin et al. 1989).

There is a difference between the OH absorption in augitic to diopsidic pyroxene with bands at 3515 cm<sup>-1</sup> (similar to that reported in Skogby et al. 1990) and 3615 cm<sup>-1</sup>, and omphacite with a main band at 3460 cm<sup>-1</sup> with a shoulder at 3515 cm<sup>-1</sup>. The 3460 cm<sup>-1</sup> is typical for omphacite (Koch-Müller et al. 2004) and likely related to the substitution of H<sup>+</sup> for Na<sup>+</sup> in the jadeite component (Bromiley and Keppler 2004). The band at 3615 cm<sup>-1</sup> can be attributed to a coupled substitution of Al<sup>3+</sup> and H<sup>+</sup> for Si on the tetrahedral site (e.g., Balan et al. 2020; Smyth et al. 1991). The interpretation of the 3515 cm<sup>-1</sup> is not straightforward and is potentially related to the coupled substitution of H<sup>+</sup> on M2-site and Ti on M1-site charge balanced by an Al on the tetrahedral site (Balan et al. 2020).

As observed for the garnet grains, the granulitic pyroxene grains display average plateau core water contents increasing from Zone I (140 µg/g) to Zone III (310 µg/g, Fig. 5) without showing any compositional changes and changes in the absorption bands. Additionally, H<sub>2</sub>O contents within one single grain increases from core to rim with different gradients for each grain. However, this H<sub>2</sub>O increase is again not accompanying a compositional change. Hence,

these findings imply that neither the water increase from Zone I to III nor from core to rim is a result of recrystallization. Consequently, this is another indication for a prograde

hydrogen diffusive process forming hydroxyl groups inside the crystal lattice and decoration of pre-existing defects. A possible mineral reaction equation for the fast hydrogen diffusion is as follows:



This reaction reduces the amount of ferric iron in pyroxene, in agreement with the observed trend in the pyroxene compositions (Table 2). Putnis et al. (2021) showed that the granulite pyroxene host amphibole lamellae along the cleavage planes. This mechanism has been discussed by several scientists and identified as another possibility to incorporate OH within a pyroxene grain (e.g., Maresch et al. 2009; Veblen and Buseck 1980, 1981). Nevertheless, the granulitic pyroxenes measured in this study do not show any high wavenumber OH features (typically at  $3670 \text{ cm}^{-1}$ , Buseck et al. 1980) that could be related to amphibole lamellae.

The omphacite in EcI hosts  $\sim 150 \mu\text{g/g}$  up to a maximum of  $\sim 425 \mu\text{g/g}$   $\text{H}_2\text{O}$ . Using SEM phase maps and examining the mineral phases directly surrounding the omphacites the  $\text{H}_2\text{O}$  contents retained in one omphacite grain can be inversely correlated with the amount of hydrous phases (Fig. 8). For cases where  $> 90 \text{ vol.}\%$  of the surrounding minerals are hydrous phases (e.g., clinozoisite, amphibole, phengite) about  $150 \mu\text{g/g}$   $\text{H}_2\text{O}$  was measured in omphacite. Contrary, for a grain with approximately  $10 \text{ vol.}\%$  of adjacent hydrous phases a maximum of  $425 \mu\text{g/g}$   $\text{H}_2\text{O}$  have been measured. The  $\text{H}_2\text{O}$  transects indicate that water contents either slightly decrease toward the rims or remain similar from core to rim. As described above the OH incorporation in clinopyroxenes is dependent on the crystallographic orientation. The analyzed omphacites crystallized during local strain and consequently,

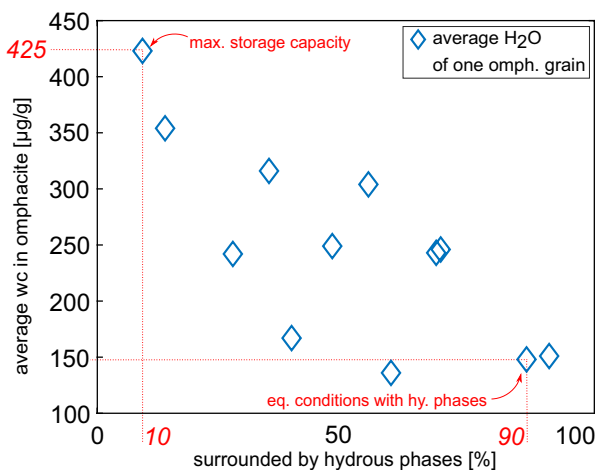


**Fig. 8** Correlation of the average water contents for each measured omphacite grain (y-axis) and the percentage of hydrous phases surrounding this grain (x-axis). The trend implies the more hydrous phases are formed next to an omphacite grain during equilibration the less water is stored or remained in the omphacite in 2-dimensional manner

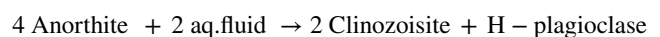
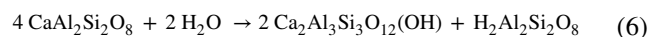
are likely aligned in the matrix of the newly formed eclogite-facies shear zone. Additionally, the omphacites are picked randomly and IR absorption spectra are comparable. The data might indicate, that newly formed omphacite grains have a maximum  $\text{H}_2\text{O}$  storage capacity of  $425 \mu\text{g/g}$  at a very small-scale (hundreds of  $\mu\text{m}$ ) local and temporary equilibrium when a free aqueous fluid is present. Low water contents of  $150 \mu\text{g/g}$  would represent the  $\text{H}_2\text{O}$  concentrations at equilibrium conditions with hydrous phases.

### Plagioclase

Several studies showed that plagioclase can incorporate water in the form of OH groups, on a range from less than 10 to more than  $500 \mu\text{g/g}$   $\text{H}_2\text{O}$  without a clear classification or trend for different plagioclase compositions and sources (e.g., Beran 1987; Johnson and Rossman 2004). It has been suggested that hydrogen is bonded to the oxygen adjacent to M-site vacancies (e.g., Mosenfelder et al. 2020; Wenk et al. 1980).

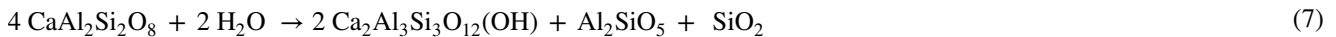
The spectra of the granulitic plagioclase have a well-defined absorption band at  $3180 \text{ cm}^{-1}$  resulting in a maximum  $\text{H}_2\text{O}$  concentration ranging from approximately  $10 \mu\text{g/g}$  for clean granulitic plagioclase in Zone I and GrI to  $\sim 140 \mu\text{g/g}$   $\text{H}_2\text{O}$  in Zone II.  $\text{H}_2\text{O}$  transects through one single plagioclase grain show irregularities in the  $\text{H}_2\text{O}$  contents from 5 to  $10 \mu\text{g/g}$  in a spot step size of  $50 \mu\text{m}$ , within range of the FTIR accuracy.

Contrary to the data of garnet and granulitic pyroxene, there are no measurement spots for granulitic plagioclase in Zone III, less in Zone II ( $n = 22$ ), and most in Zone I ( $n = 81$ ) and GrI ( $n = 156$ ), which is the result of the phase separation. The modal abundance of clinozoisite and albite-rich plagioclase increases from Zone I–III and decreases for granulitic plagioclase (Fig. 2). The findings imply that the granulitic plagioclase is the first phase that equilibrated at eclogite-facies P–T conditions once the fluid infiltrated the system. Granulitic plagioclase does not contain any ferric iron and thus,  $\text{H}_2\text{O}$  incorporation cannot operate in the same way as in pyroxene and garnet. However, there is possibly some hydrogen uptake due to the decoration of pre-existing defects as seen for the garnet and pyroxene. Nevertheless, a key observation is that in Zone I clinozoisite forms within the plagioclase without any additional quartz and kyanite. At the same time the  $\text{H}_2\text{O}$  content in plagioclase increases. These observations require the presence of an aqueous fluid and can be explained by the following reaction:



The conversion of the anorthite component of plagioclase into clinozoisite results in a shift of the plagioclase to a more albite-rich, hydrous composition. As soon as the solubility

limit for hydrogen in this plagioclase is reached, ongoing hydration will result in symplectite formation according to the reaction



where quartz and kyanite are found as reaction products in Zone II and III. This fluid-induced mineral reaction caused a recrystallization to grain sizes of about three orders of magnitude smaller, which probably significantly influenced the rock strength and hence, the ongoing rock transformation.

### Bulk water

To evaluate how much H<sub>2</sub>O was approximately absorbed by the dry granulite system the changes in the mineral assemblage from Zone I to Zone III have been correlated with the water contents of the individual phases. Average water contents for the NAMs are given in Fig. 9b. The bulk water was calculated using the modal phase abundances (Fig. 2b) for the NAMs and hydrous phases multiplied by their specific average water contents. For the hydrous phases, clinzoisite and amphibole, 2 wt.% H<sub>2</sub>O are used (e.g., Deer et al. 1997). Accordingly, the calculated bulk H<sub>2</sub>O content in the outermost part, Zone I, is around ~400 µg/g and increases up to ~2600 µg/g H<sub>2</sub>O within the eclogite-facies shear zone, Zone III. Furthest away from the shear zone (Zone I), about

35% of the bulk water is stored in NAMs, whereas in Zone

III nearly all of the water (~98%) is stored in clinzoisite and amphibole.

### Fluid influx into a metastable dry crustal rock: mechanism of hydration

Taking into account all the findings described above, it becomes evident that the granulites were most likely hydrated within three different time and length scales, including various interconnected processes occurring simultaneously. Figure 10 shows a systematic sketch of the hydration and contemporaneous eclogitization and weakening of the system:

#### T<sub>0</sub>: Initial stage

Starting from the initial stage at which the granulite precursor rock is pristine, an aqueous fluid enters the system in a highly localized fracture-like structure (e.g., Austrheim 1987; Jamtveit et al. 2019; Kaatz et al. 2021). Aqueous fluids at elevated P–T conditions as such applicable for

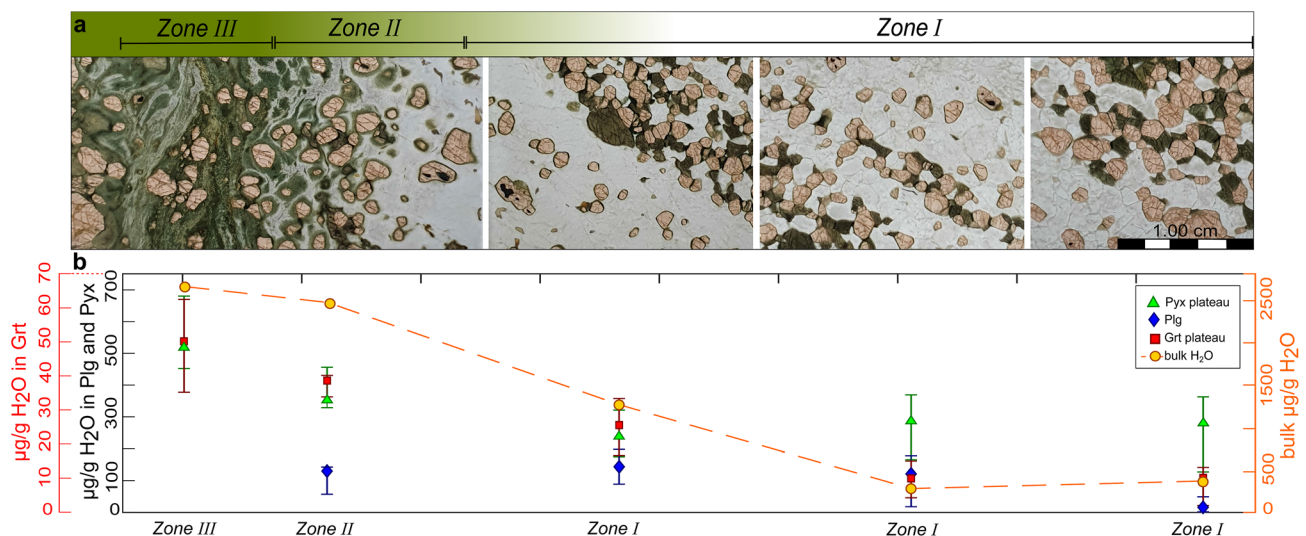


**Fig. 9** **a** Microscopic thick-section images of the analyzed profile, separated in Zone I–III. **(b)** Distribution of the average water contents for garnet, granulitic pyroxene, and granulitic plagioclase grains (y-axis on the left side). Error bars indicate variations for minimum

and maximum values of the water contents. Calculated bulk water contents are given as yellow circles (y-axis right side). The values represent Zone III, Zone II, and three sections of Zone I

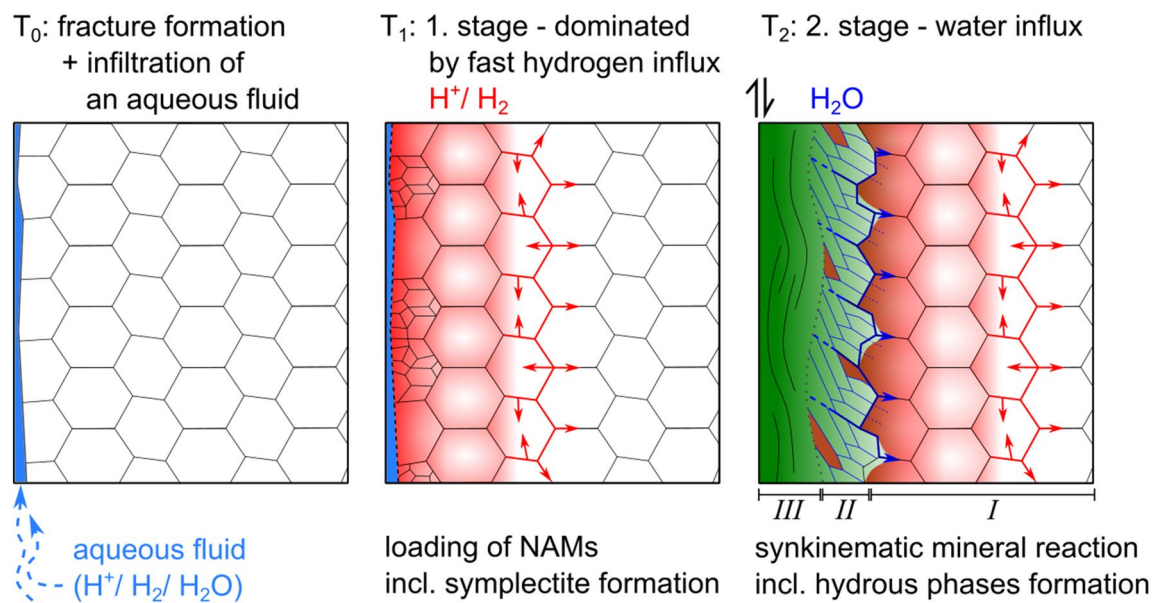


**Fig. 10** Schematic sketch of the fluid influx into the systems. The initial stage  $T_0$  is characterized by the infiltration of an aqueous fluid via a fracture-like structure. This fluid provides both  $H_2O$  and  $H^+ / H_2$ . Due to fast hydrogen diffusion  $H^+ / H_2$  pervasively propagates into the system ( $T_1$ ), loads the NAMs, induced the first formation of symplectites (albite-rich plagioclase + clinozoisite), and initiated the

equilibration of the metastable dry granulite. The slower diffusion of  $H_2O$  ( $T_2$ ) promotes reactions and pushes the synkinematic formation of eclogite-facies minerals, e.g., omphacite and hydrous phases including omphacite and probably additional clinozoisite. This finally, allowed the ductile deformation to develop the shear zone as well as Zone I to III

the eclogite-facies shear zones on Holsnøy (~2 GPa and ~700 °C; e.g., Bhowany et al. 2018) consists predominantly of  $H_2O$  but also contain trace amounts of  $H^+$  and  $H_2$  (e.g., Hermann et al. 2006; Manning 2004; Manning and Frezzotti 2020). Somehow, the rocks did not reach full equilibrium, which precludes the possibility to quantify the speciation within the infiltrating fluid. Nevertheless, according to their specific properties such as mobility and diffusivities, the influxes of the  $H_2O$  and the hydrogen develop with clearly distinct characteristics.

#### **T<sub>1</sub>: First stage—diffusion of hydrogen**

The first key observation is that garnet and granulitic pyroxene incorporate OH up to 10 cm away from the locus of fluid influx even though no direct hints of metamorphic mineral reactions are observed. Increasing core  $H_2O$  contents within the grain interiors were detected as a function of distance from Zone I to Zone III (Fig. 9b). This indicates that the grains incorporated more hydrogen as trace element in their crystal lattice the closer they have been to the fluid source, without any changes of their major element composition nor reaction with neighboring phases. The overall increase of  $H_2O$  contents in garnet and granulitic pyroxene cores has been, thus, most probably ensured by the uptake of hydrogen ( $H^+$  or  $H_2$ ), bonded to the oxygen inside the crystal lattice (Padrón-Navarta et al. 2014; Stalder et al. 2007). No

diffusion profiles have been observed related to the decoration of defects even in minerals formed in Zone I, indicating that this process is very fast. Defects are likely formed during high-temperature granulite-facies metamorphic conditions under which the wall rock was formed. Decoration of defects by hydrogen diffusion ( $H^+ / H_2$ ) in NAMs is easily achieved in laboratory experiments (Mackwell and Kohlstedt 1990; Tollan et al. 2018) but is rarely documented in natural subduction zone rocks. So far, decoration of defects in orthopyroxene has been described in fore-arc mantle xenoliths, e.g., by Tollan and Hermann (2019).

To get first-order constraints for the minimum duration of the fast hydrogen diffusion and the OH incorporation, e.g., for the garnet core plateau uplift from ~8  $\mu\text{g/g}$  (Zone I) to on average 40  $\mu\text{g/g}$  (Zone III), a diffusional hydrogen transport was modeled based on the hydrogen diffusion coefficient determined experimentally for garnet in the study of Reynes et al. (2018). Assuming a garnet grain of 1 mm in diameter at 700 °C with a starting concentration of 8  $\mu\text{g/g}$   $H_2O$ , a diffusivity of  $10^{-15}$   $\text{m}^2/\text{s}$ , a constant garnet composition and a  $H_2O$  concentration of 40  $\mu\text{g/g}$  at the garnet outermost rim, an equilibration of the garnet cores occurs within approximately two years. This minimum duration needed to produce the plateau  $H_2O$  concentrations in garnet is in agreement with results of studies that aimed to determine the duration of rock transformation due to interaction with external fluid influx (e.g., Taetz et al. 2018).

With the currently available data, it is difficult to assess whether diffusion was dominated by  $H^+$  or  $H_2$ . The neutral pH at 2 GPa and 600 °C is about 4 (Manning 2004) while  $H_2$  in aqueous fluids depends on the oxygen fugacity (Piccoli et al. 2019). An interesting side effect of extracting  $H_2$  by diffusion out of the aqueous fluid into the dry granulite is that this process will drive the dissociation reaction  $H_2O \rightarrow H_2 + \frac{1}{2} O_2$  to the right, thus leading to an increase in oxygen fugacity in the infiltrating fluid (e.g., Tollan and Hermann 2019). It is expected that this process is coupled to an increase of ferric to ferrous iron ratio (see Eq. 2), which in turn is then available for the formation and stabilization of clinozoisite (which only incorporates  $Fe^{3+}$  into its lattice) within and adjacent to the eclogite-facies shear zone. The clinozoisite displays a low ferric iron content, which slightly increases towards the shear zone (Table 1) while its abundance increases too (Figs. 2, 7). This observation provides evidence for a link between the hydration of NAMs via hydrogen diffusion in the granulite with the formation of a hydrous phase (clinozoisite) in the close vicinity of the shear zone. Additionally, the formation of clinozoisite as a result of the granulitic plagioclase breakdown lowers the average grain size of the granulitic matrix (Fig. 10).

A slightly slower process of hydrogen incorporation into NAMs is documented at the rims of granulitic pyroxene and garnet. Both minerals display bowl-shaped enrichment of  $H_2O$  contents towards the rim. Dohmen and Milke (2010) showed that volume diffusion combined with a highly efficient grain boundary diffusion generate such profiles and Tollan et al. (2018) reproduced them in decoration experiments for olivine, where they were interpreted to represent hydrogen incorporation related to slower diffusion of metal vacancies. At 700 °C, this process is about 2–3 orders of magnitude slower than the diffusion of protons (Jollands et al. 2019). The bowl-shape water content profiles in granulitic garnet and pyroxene suggest that  $H_2O$  did not diffuse out during exhumation and retrogression of the rocks.

## T<sub>2</sub>: Second stage—influx of $H_2O$ as aqueous fluid

In contrast to garnet and pyroxene, the granulitic plagioclase does not contain any ferric iron to facilitate the hydrogen uptake and thus, a different process is responsible for the hydration of plagioclase. Based on the given data and observations the suggestion is that the first fluid which arrives at the grain boundaries of the granulitic plagioclase in Zone I diffuses into the grain interiors to hydrate the plagioclase by the uptake of hydrogen due to pre-existing defects concomitant to the formation of isolated clinozoisite needles (Eq. 6). This process does not require any additional phase and is likely to proceed until the capacity of the plagioclase to absorb  $H_2O$  is reached. During further aqueous fluid infiltration, newly formed hydrous minerals control the  $H_2O$

uptake of the bulk system. The formation of additional hydrous phases, e.g., amphibole and additional clinozoisite, is restricted to narrow grain boundaries in Zone I and rather well distributed in close vicinity to the shear zone (Zone III). This shows that the influx of an aqueous fluid transforms the system from a diffusion- to a reaction-dominated regime. Based on a detailed study of isotopic resetting of micas during the partial re-equilibration of a similar rock association slightly further north within the Western Gneiss Region, Glodny et al. (2008a) concluded that the grain boundaries of the dry precursor rocks have been too dry to allow for a sufficient grain boundary-assisted element transport. Jonas et al. (2014) demonstrated that a diffusive fluid influx along formerly dry grain boundaries reflects an efficient transport mechanism for aqueous fluids into a metastable system. That leads to mineral reactions that progressively affected more and more of the grain interior by dissolution–precipitation as the fluid influx proceeds.

During the equilibration process the incorporation of OH groups either occurs in mineral phases that contain an OH-group in their structure, i.e., hydrous phases, or according to a high number of point defects that can be generated by rather fast precipitation of minerals during dissolution–precipitation reactions. This may explain, not only the  $H_2O$  content increase from the granulitic garnet cores to the eclogite-facies garnet rims but also why omphacite is able to incorporate high amounts of OH (maximum of ~425  $\mu\text{g/g}$   $H_2O$ ).

It appears that four mechanisms have been controlling the fluid influx processes: (1) fast  $H^+$ / $H_2$  grain boundary and volume diffusion, (2) decoration of pre-existing lattice defects with  $H^+$  or  $H_2$ , and (3) slower grain-boundary diffusion of  $H_2O$  causing (4) OH incorporation during reaction induced recrystallization of granulite minerals into a hydrated, new eclogite-facies mineral assemblage.

The findings of this study concerning the different length scales and rates of processes associated with an aqueous fluid infiltration are similar to those described in the context of contact metamorphism. Oxygen and hydrogen diffusion fronts show that the hydrogen always proceeded further compared to the oxygen (e.g., Andrew and O’Neil 1988; Joesten 2018; Shieh and Taylor 1969). The oxygen is exclusively transported by an aqueous fluid ( $H_2O$ ) while hydrogen ( $H^+/H_2$ ) by both, via an aqueous fluid and additional hydrogen influx. Accordingly, at bulk rock scale hydrogen proton influx is much faster and more pervasive than grain-boundary-assisted influx of an aqueous fluid, especially in a previously dry system (e.g., Dohmen and Milke 2010).

## Summary and conclusions

This study shows that NAMs play a major role in the water uptake of a dry and metastable system and are key phases to initiate, in this case, the metamorphic transformation



from granulite to eclogite while enhancing the sensitivity for ductile deformation of a rigid highly viscous bulk system. The fluid-driven eclogitization of the dry granulites on Holsnøy is mainly controlled by two distinct diffusional processes occurring contemporaneously but at different scales and rates. At first hydrogen ( $H^+/H_2$ ), which is very fast and pervasively transported through intergranular boundaries and mineral interiors, is bonded to oxygen inside the crystal lattice of a grain. Hence, OH groups are formed, which causes a “H<sub>2</sub>O-loading” of the NAMs and a H<sub>2</sub>O increase towards the eclogite-facies shear zone (fluid source) without leading necessarily to any mineral reaction. Average water contents of the garnet cores increase from ~ 10 to ~ 50 µg/g, for granulitic pyroxene from ~ 100 to ~ 310 µg/g, and for granulitic plagioclase from ~ 10 to ~ 144 µg/g. Such “H<sub>2</sub>O-loading” leads to a weakening of the granulite as well as assisted in the widening of eclogite-facies shear zones during ongoing deformation. Secondly, the influx of H<sub>2</sub>O via an aqueous fluid is mainly grain-boundary-assisted and promotes fluid–rock interaction, like the formation of hydrous phases, H<sub>2</sub>O-rich omphacite and eclogite-facies garnet rims. The bowl-shape type H<sub>2</sub>O profiles of garnet and granulitic pyroxene indicate that no hydrogen loss occurred during the exhumation of the rocks. Newly formed omphacite has a maximum H<sub>2</sub>O content of ~ 425 µg/g. Omphacite that is surrounded by a high abundance of hydrous phases has a lower H<sub>2</sub>O content of ~ 150 µg/g. The former may represent maximal water uptake capacities while the latter likely indicates the equilibrium water content within a larger volume of bulk equilibrium.

Granulitic plagioclase constitutes approximately 60 vol.% of the analyzed cross-section granulite and highly dominates the rheology, the deformation behavior, and stress resistance of the bulk system. The “H<sub>2</sub>O-loading” of the granulitic plagioclase induced by hydrogen influx triggers a two-step phase separation. In the initial step, clinozoisite needles and hydrous plagioclase form simultaneously. With ongoing hydration, plagioclase recrystallizes to an albite-rich plagioclase, kyanite and quartz with grain sizes which are about three orders of magnitude smaller. This significantly reduces the activation energy for creep mechanisms (e.g., Kohlstedt 2006), and enhances the sensitivity for ductile deformation and strain localization according to grain-size-sensitive flow laws (e.g., De Bresser et al. 2001; Hawemann et al. 2019). This temporary weakening of the system due to grain-size minimization of the plagioclase enhances the potential of new eclogite-facies shear zones to nucleate (e.g., Thielmann et al. 2015; Tullis and Yund 1985).

**Acknowledgements** This study was partially supported by the Deutsche Forschungsgemeinschaft (DFG) through grant CRC 1114 “Scaling Cascades in complex Systems,” Project Number 235221301, Project (C09)—“Dynamics of rock dehydration on multiple scales”. Julien Reynes and Jörg Hermann acknowledge financial support

by the Swiss National Science Foundation (SNSF) through grant 200021\_169062. We thank Moritz Liesegang and Hans Vrijmoed for technical support using the electron microprobe and scanning electron microscopy.

**Funding** Open Access funding enabled and organized by Projekt DEAL.

**Data availability** Supplementary material is available for authorized users.

## Declarations

**Conflict of interest** We do not have financial interests that are related to the study we submitted for publication.

**Open Access** This article is licensed under a Creative Commons Attribution 4.0 International License, which permits use, sharing, adaptation, distribution and reproduction in any medium or format, as long as you give appropriate credit to the original author(s) and the source, provide a link to the Creative Commons licence, and indicate if changes were made. The images or other third party material in this article are included in the article's Creative Commons licence, unless indicated otherwise in a credit line to the material. If material is not included in the article's Creative Commons licence and your intended use is not permitted by statutory regulation or exceeds the permitted use, you will need to obtain permission directly from the copyright holder. To view a copy of this licence, visit <http://creativecommons.org/licenses/by/4.0/>.

## References

- Aines RD, Rossman GR (1984a) The hydrous component in garnets: pyrralspites. *Am Miner* 69:1116–1126
- Aines RD, Rossman GR (1984b) Water content of mantle garnets. *Geology* 12:720–723
- Amthauer G, Rossman GR (1998) The hydrous component in andradite garnet. *Am Miner* 83:835–840
- Andersen TB, Corfu F, Labrousse L, Osmundsen P-T (2012) Evidence for hyperextension along the pre-Caledonian margin of Baltica. *J Geol Soc* 169:601–612
- Andersen TB, Jamtveit B, Dewey JF, Swensson E (1991) Subduction and eduction of continental crust: major mechanisms during continent-continent collision and orogenic extensional collapse, a model based on the south Norwegian Caledonides. *Terra Nova* 3:303–310
- Andrew A, O'Neil J (1988) Role of fluids during contact metamorphism: stable isotope evidence from the Rockley Volcanics, eastern Australia. *Am J Sc A* 288:490–511
- Austrheim H (1987) Eclogitization of lower crustal granulites by fluid migration through shear zones. *Earth Planet Sci Lett* 81:221–232
- Austrheim H (1998) Influence of fluid and deformation on metamorphism of the deep crust and consequences for the geodynamics of collision zones. When continents collide: geodynamics and geochemistry of ultrahigh-pressure rocks. Springer, Dordrecht, pp 297–323
- Austrheim H, Griffin WL (1985) Shear deformation and eclogite formation within granulite-facies anorthosites of the Bergen Arcs, western Norway. *Chem Geol* 50:267–281
- Balan E, Paulatto L, Liu J, Ingrin J (2020) Low-temperature infrared spectrum and atomic-scale structure of hydrous defects in diopside. *Eur J Mineral* 32:505–520. <https://doi.org/10.5194/ejm-32-505-2020>

- Bell DR, Ihinger PD, Rossman GR (1995) Quantitative analysis of trace OH in garnet and pyroxenes. *Am Miner* 80:465–474
- Bell DR, Rossman GR (1992) The distribution of hydroxyl in garnets from the subcontinental mantle of southern Africa. *Contrib Miner Petrol* 111:161–178
- Beran A (1987) OH groups in nominally anhydrous framework structures: an infrared spectroscopic investigation of danburite and labradorite. *Phys Chem Miner* 14:441–445
- Bhowany K, Hand M, Clark C, Kelsey D, Reddy S, Pearce M, Tucker N, Morrissey L (2018) Phase equilibria modelling constraints on P-T conditions during fluid catalysed conversion of granulite to eclogite in the Bergen Arcs, Norway. *J Metamorph Geol* 36:315–342. <https://doi.org/10.1111/jmg.12294>
- Boundy T, Fountain D, Austrheim H (1992) Structural development and petrofabrics of eclogite facies shear zones, Bergen Arcs, western Norway: implications for deep crustal deformational processes. *Contrib Miner Petrol* 10:127–146
- Boundy TM, Mezger K, Essene EJ (1997) Temporal and tectonic evolution of the granulite-eclogite association from the Bergen Arcs, western Norway. *Lithos* 39:159–178
- Bromiley GD, Keppler H (2004) An experimental investigation of hydroxyl solubility in jadeite and Na-rich clinopyroxenes. *Contrib Miner Petrol* 147:189–200. <https://doi.org/10.1007/s00410-003-0551-1>
- Buseck PR, Nord GL Jr, Veblen DR (1980) Subsolidus phenomena in pyroxenes. pyroxenes. De Gruyter, Berlin, pp 117–212
- Cawthorn RG, Collerson KD (1974) The recalculation of pyroxene end-member parameters and the estimation of ferrous and ferric iron content from electron microprobe analyses. *Am Mineralogist: J Earth Planet Mater* 59:1203–1208
- Cohen-Addad C, Ducros P, Bertaut E (1967) Étude de la substitution du groupement SiO<sub>4</sub> par (OH) 4 dans les composés Al<sub>2</sub>Ca<sub>3</sub>(OH) 12 et Al<sub>2</sub>Ca<sub>3</sub>(SiO<sub>4</sub>) 2, 16 (OH) 3, 36 de type grenat. *Acta Crystallogr A* 23:220–230
- Corfu F, Andersen TB, Gasser D (2014) The Scandinavian Caledonides: main features, conceptual advances and critical questions. Geological Society, London, Special Publications 390:9–43. <https://doi.org/10.1144/SP390.25>
- De Bresser J, Ter Heege J, Spiers C (2001) Grain size reduction by dynamic recrystallization: can it result in major rheological weakening? *Int J Earth Sci* 90:28–45. <https://doi.org/10.1007/s005310000149>
- Deer WA, Howie RA, Zussman J (1997) Rock-forming minerals: single-chain silicates, vol 2A. Geological Society of London, London
- Dohmen R, Milke R (2010) Diffusion in polycrystalline materials: grain boundaries, mathematical models, and experimental data. *Rev Mineral Geochem* 72:921–970. <https://doi.org/10.2138/rmg.2010.72.21>
- Fossen H, Dunlap WJ (1998) Timing and kinematics of Caledonian thrusting and extensional collapse, southern Norway: evidence from <sup>40</sup>Ar/<sup>39</sup>Ar thermochronology. *J Struct Geol* 20:765–781. [https://doi.org/10.1016/S0191-8141\(98\)00007-8](https://doi.org/10.1016/S0191-8141(98)00007-8)
- Fountain DM, Boundy TM, Austrheim H, Rey P (1994) Eclogite-facies shear zones—deep crustal reflectors? *Tectonophysics* 232:411–424. [https://doi.org/10.1016/0040-1951\(94\)90100-7](https://doi.org/10.1016/0040-1951(94)90100-7)
- Geiger CA, Langer K, Bell DR, Rossman GR, Winkler B (1991) The hydroxide component in synthetic pyrope. *Am Miner* 76:49–59
- Geiger CA, Rossman GR (2020) Micro- and nano-size hydrogarnet clusters and proton ordering in calcium silicate garnet: Part I. The quest to understand the nature of “water” in garnet continues. *Ame Mineralogist: J Earth Planetary Mater* 105:455–467. <https://doi.org/10.2138/am-2020-7256>
- Glodny J, Kühn A, Austrheim H (2008a) Diffusion versus recrystallization processes in Rb–Sr geochronology: isotopic relics in eclogite facies rocks, Western Gneiss Region, Norway. *Geochim Cosmochim Acta* 72:506–525. <https://doi.org/10.1016/j.gca.2007.10.021>
- Glodny J, Kühn A, Austrheim H (2008b) Geochronology of fluid-induced eclogite and amphibolite facies metamorphic reactions in a subduction–collision system, Bergen Arcs, Norway. *Contrib Miner Petrol* 156:27–48. <https://doi.org/10.1007/s00410-007-0272-y>
- Hawemann F, Mancktelow NS, Pennacchioni G, Wex S, Camacho A (2019) Weak and slow, strong and fast: how shear zones evolve in a dry continental crust (Musgrave Ranges, Central Australia). *J Geophys Res: Solid Earth* 124:219–240. <https://doi.org/10.1029/2018JB016559>
- Hermann J, Spandler C, Hack A, Korsakov AV (2006) Aqueous fluids and hydrous melts in high-pressure and ultra-high pressure rocks: implications for element transfer in subduction zones. *Lithos* 92:399–417. <https://doi.org/10.1016/j.lithos.2006.03.055>
- Ingrin J, Latrous K, Doukhan JC, Doukhan N (1989) Water in diopside: an electron microscopy and infrared spectroscopy study. *Eur J Mineral* 327–342
- Jakob J, Alsaif M, Corfu F, Andersen TB (2017) Age and origin of thin discontinuous gneiss sheets in the distal domain of the magma-poor hyperextended pre-Caledonian margin of Baltica, southern Norway. *J Geol Soc* 174:557–571. <https://doi.org/10.1144/jgs2016-049>
- Jakob J, Andersen TB, Kjøl HJ (2019) A review and reinterpretation of the architecture of the south and south-central Scandinavian Caledonides—A magma-poor to magma-rich transition and the significance of the reactivation of rift inherited structures. *Earth-Sci Rev* 192:513–528
- Jamtveit B, Ben-Zion Y, Renard F, Austrheim H (2018a) Earthquake-induced transformation of the lower crust. *Nature* 556:487–491. <https://doi.org/10.1029/2018JB016461>
- Jamtveit B, Bucher-Nurminen K, Austrheim H (1990) Fluid controlled eclogitization of granulites in deep crustal shear zones, Bergen arcs, Western Norway. *Contrib Mineral Petrol* 104:184–193
- Jamtveit B, Moulas E, Andersen TB, Austrheim H, Corfu F, Petley-Ragan A, Schmalholz SM (2018b) High pressure metamorphism caused by fluid induced weakening of deep continental crust. *Sci Rep* 8:17011. <https://doi.org/10.1038/s41598-018-35200-1>
- Jamtveit B, Petley-Ragan A, Incel S, Dunkel KG, Aupart C, Austrheim H, Corfu F, Menegon L, Renard F (2019) The effects of earthquakes and fluids on the metamorphism of the lower continental crust. *J Geophys Res: Solid Earth* 124:7725–7755. <https://doi.org/10.1029/2018JB016461>
- Joesten RL (2018) Kinetics of coarsening and diffusion-controlled mineral growth. *Contact Metamorph*. <https://doi.org/10.1515/9781501509612-014>
- John T, Schenk V (2003) Partial eclogitization of gabbroic rocks in a late Precambrian subduction zone (Zambia): prograde metamorphism triggered by fluid infiltration. *Contrib Miner Petrol* 146:174–191. <https://doi.org/10.1007/s00410-003-0492-8>
- Johnson EA (2006) Water in nominally anhydrous crustal minerals: speciation, concentration, and geologic significance. *Rev Mineral Geochem* 62:117–154. <https://doi.org/10.2138/rmg.2006.62.6>
- Johnson EA, Rossman GR (2003) The concentration and speciation of hydrogen in feldspars using FTIR and <sup>1</sup>H MAS NMR spectroscopy. *Am Miner* 88:901–911. <https://doi.org/10.2138/am-2003-5-620>
- Johnson EA, Rossman GR (2004) A survey of hydrous species and concentrations in igneous feldspars. *Am Miner* 89:586–600. <https://doi.org/10.2138/am-2004-0413>
- Jolivet L, Raimbourg H, Labrousse L, Avigad D, Leroy Y, Austrheim H, Andersen TB (2005) Softening triggered by eclogitization, the first step toward exhumation during continental subduction. *Earth Planet Sci Lett* 237:532–547. <https://doi.org/10.1016/j.epsl.2005.06.047>
- Jollands MC, Kempf E, Hermann J, Müntener O (2019) Coupled inter-site reaction and diffusion: rapid dehydrogenation of

- silicon vacancies in natural olivine. *Geochim Cosmochim Acta* 262:220–242
- Jollands MC, O'Neill HSC, Berry AJ, Le Losq C, Rivard C, Hermann J (2021) A combined fourier transform infrared and Cr K-edge X-ray absorption near-edge structure spectroscopy study of the substitution and diffusion of H in Cr-doped forsterite. *Eur J Mineral* 33:113–138
- Jonas L, John T, King HE, Geisler T, Putnis A (2014) The role of grain boundaries and transient porosity in rocks as fluid pathways for reaction front propagation. *Earth Planet Sci Lett* 386:64–74. <https://doi.org/10.1016/j.epsl.2013.10.050>
- Kaatz L, Zertani S, Moulas E, John T, Labrousse L, Schmalholz SM, Andersen TB (2021) Widening of hydrous shear zones during incipient eclogitization of metastable dry and rigid lower crust—Holsnøy, western Norway. *Tectonics*. <https://doi.org/10.1029/2020TC006572>
- Katayama I, Nakashima S, Yurimoto H (2006) Water content in natural eclogite and implication for water transport into the deep upper mantle. *Lithos* 86:245–259. <https://doi.org/10.1016/j.lithos.2005.06.006>
- Koch-Müller M, Matsyuk SS, Wirth R (2004) Hydroxyl in omphacites and omphacitic clinopyroxenes of upper mantle to lower crustal origin beneath the Siberian platform. *Am Miner* 89:921–931. <https://doi.org/10.2138/am-2004-0701>
- Kohlstedt DL (2006) The role of water in high-temperature rock deformation. *Rev Mineral Geochem* 62:377–396. <https://doi.org/10.2138/rmg.2006.62.16>
- Kovács I, Oneill HSC, Hermann JR, Hauri EH (2010) Site-specific infrared OH absorption coefficients for water substitution into olivine. *Am Mineral* 95:292–299. <https://doi.org/10.2138/am.2010.3313>
- Kühn A, Glodny J, Austrheim H, Råheim A (2002) The Caledonian tectono-metamorphic evolution of the Lindås Nappe: constraints from U-Pb, Sm-Nd and Rb-Sr ages of granitoid dykes. *Nor J Geol/Nor Geol Foren* 82:45–57
- Mackwell SJ, Kohlstedt DL (1990) Diffusion of hydrogen in olivine: implications for water in the mantle. *J Geophys Res: Solid Earth* 95:5079–5088
- Malvoisin B, Austrheim H, Hetényi G, Reynes J, Hermann J, Baumgartner LP, Podladchikov YY (2020) Sustainable densification of the deep crust. *Geology* 48(7):673–677
- Manning CE (2004) The chemistry of subduction-zone fluids. *Earth Planet Sci Lett* 223:1–16. <https://doi.org/10.1016/j.epsl.2004.04.030>
- Manning CE, Frezzotti ML (2020) Subduction-zone fluids. elements: an international magazine of mineralogy. *Geochem Petrology* 16:395–400. <https://doi.org/10.2138/gselements.16.6.395>
- Maresch W, Welch M, Gottschalk M, Ruthmann W, Czank M, Ashbrook S (2009) Synthetic amphiboles and triple-chain silicates in the system Na<sub>2</sub>O-MgO-SiO<sub>2</sub>-H<sub>2</sub>O: phase characterization, compositional relations and excess H. *Mineral Mag* 73:957–996. <https://doi.org/10.1180/minmag.2009.073.6.957>
- Mattey D, Jackson D, Harris N, Kelley S (1994) Isotopic constraints on fluid infiltration from an eclogite facies shear zone, Holsenøy, Norway. *J Metamorph Geol* 12:311–325
- Menegon L, Pennacchioni G, Malaspina N, Harris K, Wood E (2017) Earthquakes as precursors of ductile shear zones in the dry and strong lower crust. *Geochem Geophys Geosyst* 18:4356–4374
- Morimoto N (1988) Nomenclature of pyroxenes. *Mineral Petrol* 39:55–76
- Mosenfelder JL, Andrys JL, von der Handt A, Kohlstedt DL, Hirschmann MM (2020) Hydrogen incorporation in plagioclase. *Geochim Cosmochim Acta*. <https://doi.org/10.1016/j.gca.2020.03.013>
- Padrón-Navarta JA, Hermann J, O'Neill HSC (2014) Site-specific hydrogen diffusion rates in forsterite. *Earth Planet Sci Lett* 392:100–112. <https://doi.org/10.1016/j.epsl.2014.01.055>
- Petley-Ragan A, Dunkel KG, Austrheim H, Ildefonse B, Jamtveit B (2018) Microstructural records of earthquakes in the lower crust and associated fluid-driven metamorphism in plagioclase-rich granulites. *J Geophys Res: Solid Earth* 123:3729–3746. <https://doi.org/10.1029/2017JB015348>
- Piccoli F, Hermann J, Pettke T, Connolly J, Kempf ED, Duarte JV (2019) Subducting serpentinites release reduced, not oxidized, aqueous fluids. *Sci Rep* 9:1–7
- Putnis A, Austrheim H (2010) Fluid-induced processes: metasomatism and metamorphism. *Geofluids*. <https://doi.org/10.1111/j.1468-8123.2010.00285.x>
- Putnis A, John T (2010) Replacement processes in the Earth's crust. *Elements* 6:159–164. <https://doi.org/10.2113/gselements.6.3.159>
- Putnis A, Moore J, Prent AM, Beinlich A, Austrheim H (2021) Preservation of granulite in a partially eclogitized terrane: Metastable phenomena or local pressure variations? *Lithos*. <https://doi.org/10.1016/j.lithos.2021.106413>
- Raimbourg H, Goffé B, Jolivet L (2007) Garnet reequilibration and growth in the eclogite facies and geodynamical evolution near peak metamorphic conditions. *Contrib Miner Petrol* 153:1–28. <https://doi.org/10.1007/s00410-006-0130-3>
- Raimbourg H, Jolivet L, Labrousse L, Leroy Y, Avigad D (2005) Kinematics of syneclogite deformation in the Bergen Arcs, Norway: implications for exhumation mechanisms. *Geol Soc, Lond, Spec Publ* 243:175–192. <https://doi.org/10.1144/GSL.SP.2005.243.01.13>
- Reynes J, Jollands M, Hermann J, Ireland T (2018) Experimental constraints on hydrogen diffusion in garnet. *Contrib Miner Petrol* 173:69. <https://doi.org/10.1007/s00410-018-1492-z>
- Roberts D (2003) The Scandinavian Caledonides: event chronology, palaeogeographic settings and likely modern analogues. *Tectonophysics* 365:283–299. [https://doi.org/10.1016/S0040-1951\(03\)00026-X](https://doi.org/10.1016/S0040-1951(03)00026-X)
- Rondenay S, Abers GA, van Keken PE (2008) Seismic imaging of subduction zone metamorphism. *Geology*. <https://doi.org/10.1130/G24112A.1>
- Schmid R, Altenberger U, Oberhänsli R (1998) Polyphase tectono-metamorphic evolution of the northwestern Lindås Nappe on Holsnøy. Bergen Arcs, Caledonides, SW-Norway
- Shieh Y, Taylor H (1969) Oxygen and hydrogen isotope studies of contact metamorphism in the Santa Rosa Range, Nevada and other areas. *Contrib Miner Petrol* 20:306–356
- Skogby H (2006) Water in natural mantle minerals I: pyroxenes. *Rev Mineral Geochem* 62:155–167. <https://doi.org/10.2138/rmg.2006.62.7>
- Skogby H, Bell DR, Rossman GR (1990) Hydroxide in pyroxene: variations in the natural environment. *Am Miner* 75:764–774
- Smyth J, Bell D, Rossman G (1991) Incorporation of hydroxyl in upper-mantle clinopyroxenes. *Nature* 351:732–735
- Stalder R, Purwin H, Skogby H (2007) Influence of Fe on hydrogen diffusivity in orthopyroxene. *Eur J Mineral* 19:899–903. <https://doi.org/10.1127/0935-1221/2007/0019-1780>
- Taetz S, John T, Bröcker M, Spandler C, Stracke A (2018) Fast intraslab fluid-flow events linked to pulses of high pore fluid pressure at the subducted plate interface. *Earth Planet Sci Lett* 482:33–43
- Thielmann M, Rozel A, Kaus B, Ricard Y (2015) Intermediate-depth earthquake generation and shear zone formation caused by grain size reduction and shear heating. *Geology* 43:791–794. <https://doi.org/10.1130/G36864.1>
- Tollan P, Hermann J (2019) Arc magmas oxidized by water dissociation and hydrogen incorporation in orthopyroxene. *Nat Geosci* 12:667–671

- Tollan PM, O'Neill HSC, Hermann J (2018) The role of trace elements in controlling H incorporation in San Carlos olivine. *Contrib Miner Petrol* 173:1–23
- Tullis J, Yund RA (1985) Dynamic recrystallization of feldspar: a mechanism for ductile shear zone formation. *Geology* 13:238–241. [https://doi.org/10.1130/0091-7613\(1985\)13%3C238:DROFAM%3E2.0.CO;2](https://doi.org/10.1130/0091-7613(1985)13%3C238:DROFAM%3E2.0.CO;2)
- Veblen DR, Buseck PR (1980) Microstructures and reaction mechanisms in biopyriboles. *Am Miner* 65:599–623
- Veblen DR, Buseck PR (1981) Hydrous pyriboles and sheet silicates in pyroxenes and uralites: intergrowth microstructures and reaction mechanisms. *Am Miner* 66:1107–1134
- Wayte GJ, Worden RH, Rubie DC, Droop GT (1989) A TEM study of disequilibrium plagioclase breakdown at high pressure: the role of infiltrating fluid. *Contrib Miner Petrol* 101:426–437
- Wenk H, Joswig W, Tagai T, Korekawa M, Smith BK (1980) The average structure of An 62–66 labradorite. *Am Miner* 65:81–95
- Yuan X, Sobolev SV, Kind R, Oncken O, Bock G, Asch G, Schurr B, Graeber F, Rudloff A, Hanka WJN (2000) Subduction and collision processes in the central andes constrained by converted seismic phases. *Nature* 408:958
- Zertani S, Labrousse L, John T, Andersen TB, Tilmann F (2019) The Interplay of eclogitization and deformation during deep burial of the lower continental crust—a case study from the Bergen arcs (Western Norway). *Tectonics*. <https://doi.org/10.1029/2018TC005297>
- Zertani S, Vrijmoed JC, Tilmann F, John T, Andersen TB, Labrousse L (2020) P wave anisotropy caused by partial eclogitization of descending crust demonstrated by modeling effective petrophysical properties. *Geochem Geophys Geosyst*. <https://doi.org/10.1029/2019GC008906>

**Publisher's Note** Springer Nature remains neutral with regard to jurisdictional claims in published maps and institutional affiliations.